

Form generation of rigid origami for approximation of a curved surface based on mechanical property of partially rigid frames

Kentaro Hayakawa^{a,*}, Makoto Ohsaki^a

^a*Department of Architecture and Architectural Engineering, Kyoto University, Kyoto-Daigaku Katsura, Nishikyo, Kyoto 615-8540, Japan*

Abstract

A method is presented for approximating a curved surface by a developable rigid origami; a polyhedral shape which can be developed to a plane without deformation of its facets. Form generation starts from a triangulated surface, and an optimization problem is solved to obtain a polyhedron which satisfies the geometric conditions for developability. The degrees of freedom of a rigid origami mechanism with only triangular facets are often too large for the engineering application, and therefore, it is sequentially reduced by fixing (removing) some crease lines, along which the rigid facets rotate. However, the crease line that is not fixed often becomes unable to rotate in the process of fixing the crease lines; consequently, the polyhedron cannot be developed to a plane. To avoid such an unfavorable locking situation, selection criteria of the crease line to be fixed are proposed. They are defined based on the eigenvalues and their derivatives of the stiffness matrix of the frame model, which is the numerical model for form generation and mechanism analysis of rigid origami. The performance of the proposed criteria is demonstrated through the examples of surfaces with some patterns of crease lines.

Keywords: Rigid origami, Form generation, Optimization, Deformation mechanism, Partially rigid frame

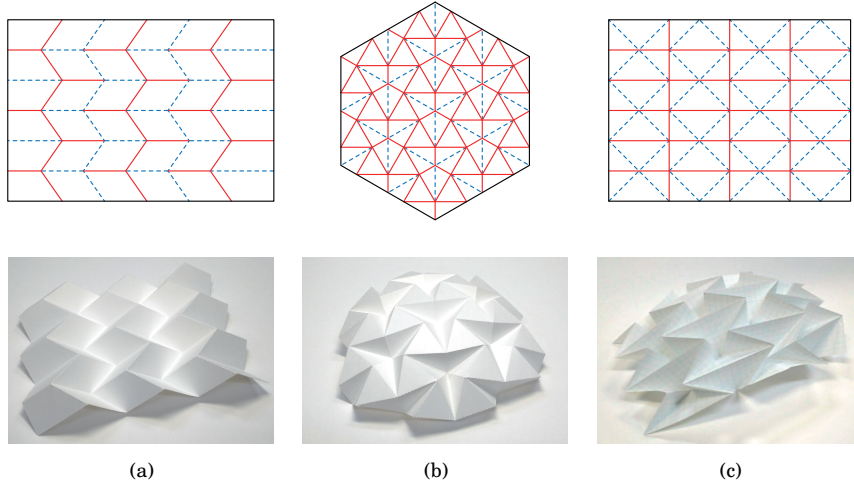


Figure 1: Typical crease patterns (paper models are created by the authors): (a) Miura-ori; (b) Resch's pattern; (c) waterbomb tessellation

1. Introduction

Rigid origami is a type of polyhedral origami whose deformation is concentrated on the crease lines during the folding and unfolding processes without in-plane or out-of-plane deformation of each facet. Such a deformation mechanism is called a *rigid-foldable* mechanism, which is determined only by the arrangement of crease lines, i.e., by the crease pattern, and the facets and crease lines can be substituted with rigid panels and rotational hinges, respectively. This property is very suitable for engineering applications. It is well known that Miura-ori, which is a rigid-foldable quadrilateral crease pattern, has been applied to the foldable solar panels mounted on artificial satellites [1], and also to the maps which can be folded compactly [2]. Recently, many attempts have been made to apply the deformation mechanism of rigid origami to a variety of purposes in various scales such as medical equipment [3] and building structures [4]. Particularly in the field of architecture, a rigid-foldable mechanism has been introduced into a spatial structure such as a dome to develop an easy and safe construction method like Pantadome [5]. In addition, rigid origami is expected to realize a temporary structure that is portable and easy to be assembled to a foldable shelter [6, 7].

*Corresponding author

Email addresses: se.hayakawa@arch.kyoto-u.ac.jp (Kentaro Hayakawa), ohsaki@arch.kyoto-u.ac.jp (Makoto Ohsaki)

For the application of rigid origami to architectural purposes, it is necessary to satisfy various demands reflecting the floor planning and the environment of the structure. Therefore, it is important to generate a rigid-foldable shape which is the same as or close to the desired shape. In this paper, the target curved surface is approximated by a developable and rigid-foldable origami. A frame model is used for the design and the mechanism analysis of the rigid origami. The degrees of freedom (DOFs) of the folding mechanism is reduced by fixing (removing) some crease lines, and the crease lines to be fixed are selected based on the eigenvalues and their derivatives of the stiffness matrix of the frame model.

Various methods have been proposed for generating rigid origami with a generic configuration by generalizing a well-known rigid-foldable regular crease pattern; e.g. Dudte *et al.* [8] and Song *et al.* [9] used Miura-ori [1] as shown in Fig. 1(a), Tachi [10] used Resch’s pattern [11] in Fig. 1(b), Zhao *et al.* [12] used waterbomb tessellation in Fig. 1(c) and Wu [13] used Yoshimura pattern. The necessary and sufficient condition for the rigid-foldability of a quadrilateral mesh is derived by Tachi [14, 15]. It is also called the loop condition and expressed for the angles between the crease lines and the angles between the normal vectors of the pairs of adjacent facets connected to crease lines. Based on the loop condition, Tachi generated a general shaped rigid origami with degree-four vertices using Miura-ori, discrete Voss surface [16], or the combination of them as the initial shape. He and Guest [17, 18] proposed a method for form generation of a rigid-foldable quadrilateral mesh without relying on typical crease patterns such as Miura-ori. However, each of the methods described above can handle each specific crease pattern, and cannot generate various crease patterns. Furthermore, since the deformation mechanism of rigid origami is determined only by its crease pattern, it is difficult to obtain various shapes with different DOFs.

In recent studies [19, 20, 21], the authors proposed a method for form generation of rigid origami using an optimization method that does not depend on the typical crease patterns. A developable and rigid-foldable polyhedral surface can be obtained by using their method. It approximates an open curved surface of an arbitrary shape. An optimization problem is formulated to minimize the sum of the squares of discrete Gaussian curvature defined at the interior vertices as the angle defect [22] so that the polyhedron has zero Gaussian curvature at each interior vertex and is developable to a plane. The initial shape of the optimization process is the triangulated target surface. However, a polyhedron with only triangular facets has a very large number of DOFs. This is undesirable in view of engineering application because the mechanism cannot be stabilized by simply supporting a part

of the structure and the rotation of the crease lines should be constrained to maintain the curved polyhedral shape. Therefore, some crease lines are to be sequentially fixed (removed) to reduce the DOF. The adjacent facets connected to each fixed crease line are integrated into a flat facet with more than three vertices. The n -gonal flat facet ($n > 3$) is formed by adding the squared norm of the cross product of their unit normal vectors to the objective function of the optimization problem. The crease lines to be fixed are selected based on the angles between the facets connected to them. By solving the optimization problem multiple times while increasing the number of fixed crease lines, multiple optimal shapes with the different DOFs can be obtained. However, when an inappropriate crease line is fixed in the process of form generation, some crease lines that are not fixed often become unable to rotate, that is to say, the crease lines are *locked*. The facets connecting to the locked crease line cannot rotate around it even though they are not coplanar and the polyhedron cannot be developed to a plane without deformation of its facets. Therefore, it is necessary to prevent crease lines being locked, and the crease line to be fixed is selected again if any locked crease line exists, which leads to a complex try-and-error process.

A frame model also has been developed in the authors' previous studies for the use in form generation and analysis of deformation mechanism. Although the truss model [23, 24] and the rotational hinge model [25, 26] have often been employed to design and analysis of rigid origami, they have some drawbacks. The former is composed of pin-jointed bars mainly located at the edges of a polyhedron and the variables of the analysis are the positions of its nodes. To prevent deformation of the facet with more than three vertices, it is necessary to locate the bars not only in the diagonal direction but also in the shape of a polygonal pyramid or to assign additional components to the stiffness matrix of the facet to prevent the out-of-plane deformation. The latter is composed of rigid panels connected by hinges, and the rotation angles of the hinges are the variables. Although the folded state is easily described by the folding angles, the rotational hinge model is not suitable to the purpose of this paper; i.e. form generation and analysis of deformation mechanism of the rigid origami. The angles between the adjacent crease lines and the global scale of the polyhedron should be included in design variables to uniquely determine the shape of the polyhedron, and the complicated constraints on the variables are necessary to make these angles compatible. Therefore, using these variables is impractical since the 3D positions of the vertices are very complicated expressions of the angles. It would be difficult and inefficient to enforce constraints on positions of the vertices such as their displacement ranges in the optimization problem using the rotational hinge model. In ad-

dition, complex shell elements should be used with hinges to construct the finite element model, and it is difficult to trace the large deformation process using a general finite element analysis software; therefore, a special software such as *Rigid Origami Simulator* developed by Tachi [25] is needed to trace the deformation process of rigid origami. To overcome these drawbacks, the authors developed a frame model [19, 20, 21] to carry out the form generation and mechanism analysis without reconstruction of the model and conversion of the variables. The method for stability analysis and finding mechanism of partially rigid frames which have arbitrary inclined hinges [27, 28] is simply applied to the evaluation of the infinitesimal mechanism of a frame model. Large deformation analysis can be easily carried out using a general finite element analysis software to investigate the existence of the finite mechanism.

In this paper, a method is proposed for predicting the transition of the deformation mechanism of rigid origami due to choosing and fixing some crease lines. It is predicted based on the eigenvalues and their derivatives of the stiffness matrix which is assembled using the rigid-folding modes derived from the compatibility matrix of the frame model and the fictitious stiffness of the hinges. Two selection criteria of the crease lines to be fixed are introduced to avoid undesirable locking of crease lines. By using a criterion introduced in this paper, the number of solution processes of optimization during form generation is reduced and the computational efficiency for form generation is improved. This paper is mainly divided into three parts. The first part consists of Sections 2 and 3 and describes the process of form generation based on the geometrical property of the frame model. The second part consists of Sections 4 and 5 and investigates properties of rigid-fold mechanism based on the mechanics of the frame model. The third part shows numerical examples in Section 6. In Section 2, the configuration of a frame model is shown and compatibility equations about the positions of nodes are derived to ensure that the corresponding polyhedron is calculated consistently from the nodal coordinates of the frame. An optimization problem for form generation is formulated and a procedure for generating a rigid-foldable origami with small DOF is shown in Section 3. In Section 4, the change of the deformation mechanism is predicted based on the rigid-folding modes derived using the singular value decomposition (SVD) of the matrix representing the equilibrium equations of frames and the constraints on the moment around the rotational axes of hinges that have artificial small stiffnesses. Based on the result in Section 4, the selection criteria of the crease lines to be fixed are formulated in Section 5. The effectiveness of the proposed criteria is demonstrated in Section 6 by comparing the results of form generation of target surfaces with some types of crease patterns using the proposed and other se-

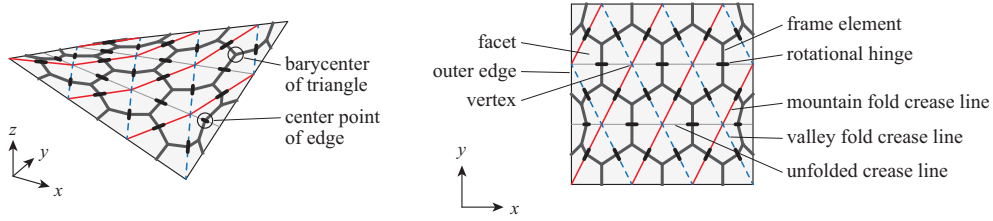


Figure 2: Configuration of a polyhedron with triangular facets and a frame model

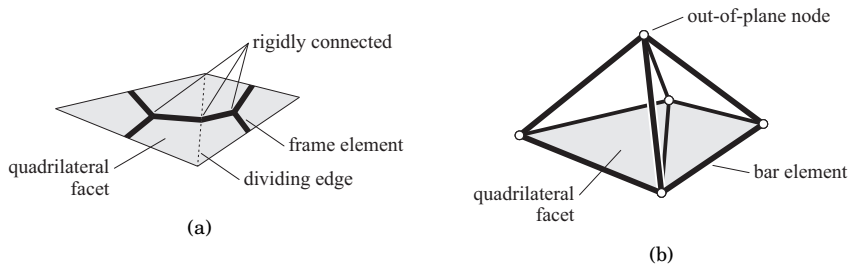


Figure 3: Configuration of a quadrilateral facet: (a) truss model; (b) frame model

lection criteria. In addition, development diagrams are generated for optimal shapes, and large deformation analyses are carried out to confirm that the obtained solution can be developed to a plane through a rigid-folding motion.

2. Frame model

In this paper, a form-finding method is presented for a *polyhedron* approximating a curved surface. A polyhedron consists of *vertices*, *edges*, and *facets* (Fig. 2). Edges are classified into *crease lines* around which facets rotate (Fig. 2), *dividing edges* which divide a facet with four or more vertices into triangles (Fig. 3), and *outer edges* on the outer boundary of the polyhedron as shown in Figs. 2 and 3. In other words, a facet is bounded by coplanar crease lines and outer edges, and it is composed of several triangles connected by dividing edges if it has more than three vertices. When a crease line is fixed (removed) in the process of form generation, it becomes a dividing edge, i.e. *fixed crease line*. Furthermore, crease lines are classified into *mountain fold crease lines*, *valley fold crease lines*, and *unfolded crease lines* (Fig. 2). A mountain fold crease line forms a "protruding ridge", and a valley fold crease line forms an "indented trough" [29]. If two facets are connected to an unfolded crease line, they are parallel. Mountain fold crease lines, valley fold crease lines, and unfolded crease lines are represented by solid lines, dotted lines, and

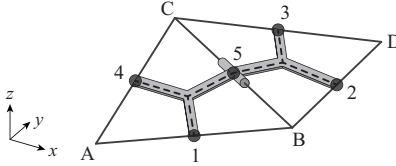


Figure 4: A pair of triangles connected by a hinge

thin lines, respectively in Fig. 2. In this study, a frame model [19, 20, 21] is used for the form generation and the analysis of the deformation mechanism of rigid origami. It consists of the frame elements represented by the bold lines in Fig. 2. Frame elements are connected by the hinge on each crease line and rigidly connected on each dividing edge and at the arbitrary points on the facets. The end point of a frame element is called *node*, and it is distinguished from the vertex. A node on the edge of the polyhedron is located at the center point of the edge. The position of a node on the facet can be arbitrarily specified, and in this study, the node is located at the barycenter of each triangle facet including the triangle constituting the facet with more than three vertices. Since the frame elements are rigidly connected on the facet, the out-of-plane stiffness of the facet with more than three vertices can be ensured without assembling a complicated configuration. For example, a node outside of the plane and additional bar elements are necessary to model a quadrilateral facet by the truss model as shown in Fig. 3(b). On the other hand, using a frame model, rigid origami can be represented by fewer elements than using an truss model as shown in Fig. 3(a). The number of infinitesimal deformation mechanism is examined by using the method for the analysis of kinematic indeterminacy of partially rigid frames [27, 28]. The detail of the method is shown in Section 4 and Appendix A. Furthermore, it is necessary to investigate not only the infinitesimal deformation mechanism but also the large-deformation mechanism in order to confirm that the obtained rigid origami model can be continuously developed and folded. Large deformation analysis can be easily carried out using the standard beam and hinge elements of a general finite element analysis software.

The variables in the process of form generation are the coordinates of the nodes of frame model on the triangle edges of polyhedron. They cannot be set arbitrarily, because they must satisfy the compatibility conditions so that the coordinates of the vertices of the corresponding polyhedron are calculated consistently. The compatibility conditions reflect the connection of the edges of the polyhedron. For the adjacent triangles ABC and BDC as shown in Fig. 4, the coordinates of vertices B and C can be expressed in two ways using

the coordinates of nodes 1, 4, 5 and 2, 3, 5. Let x_i^v, y_i^v and z_i^v denote x -, y - and z -coordinates of vertex i ($i \in B, C$), respectively, and x_j^e, y_j^e and z_j^e denote x -, y - and z -coordinates of node j ($j = 1, \dots, 5$), respectively. Then the coordinates of vertices B and C are expressed as follows since a node on the edge is located at the center point of the edge:

$$\begin{cases} x_B^v = x_5^e + x_1^e - x_4^e = x_5^e + x_2^e - x_3^e \\ x_C^v = x_5^e - x_1^e + x_4^e = x_5^e - x_2^e + x_3^e \\ y_B^v = y_5^e + y_1^e - y_4^e = y_5^e + y_2^e - y_3^e \\ y_C^v = y_5^e - y_1^e + y_4^e = y_5^e - y_2^e + y_3^e \\ z_B^v = z_5^e + z_1^e - z_4^e = z_5^e + z_2^e - z_3^e \\ z_C^v = z_5^e - z_1^e + z_4^e = z_5^e - z_2^e + z_3^e \end{cases} \quad (1)$$

Therefore, the following equations hold:

$$\begin{cases} x_1^e - x_2^e + x_3^e - x_4^e = 0 \\ y_1^e - y_2^e + y_3^e - y_4^e = 0 \\ z_1^e - z_2^e + z_3^e - z_4^e = 0 \end{cases} \quad (2)$$

Let V and E denote the numbers of vertices and edges of the polyhedron, respectively. The E -dimensional vectors $\mathbf{x}^e, \mathbf{y}^e$, and \mathbf{z}^e consisting of x_i^e, y_i^e , and z_i^e ($i = 1, \dots, E$), respectively, satisfy the compatibility equations derived from Eq. (2) for all the interior edges, which can be formulated using a full rank matrix $\mathbf{C} \in \mathbb{R}^{(E-V) \times E}$ as follows [21]:

$$\begin{cases} \mathbf{C}\mathbf{x}^e = \mathbf{0} \\ \mathbf{C}\mathbf{y}^e = \mathbf{0} \\ \mathbf{C}\mathbf{z}^e = \mathbf{0} \end{cases} \quad (3)$$

The number of independent x -coordinates of the nodes on edges is equal to V , and \mathbf{x}^e can be divided into $\bar{\mathbf{x}}^e \in \mathbb{R}^V$ consisting of independent x -coordinates and $\hat{\mathbf{x}}^e \in \mathbb{R}^{E-V}$ consisting of dependent x -coordinates. According to the first equation of Eq. (3), $\hat{\mathbf{x}}^e$ can be calculated from $\bar{\mathbf{x}}^e$ as

$$\begin{aligned} [\hat{\mathbf{C}} \quad \bar{\mathbf{C}}] \begin{pmatrix} \hat{\mathbf{x}}^e \\ \bar{\mathbf{x}}^e \end{pmatrix} &= \hat{\mathbf{C}}\hat{\mathbf{x}}^e + \bar{\mathbf{C}}\bar{\mathbf{x}}^e = \mathbf{0} \\ \Rightarrow \hat{\mathbf{x}}^e &= -\hat{\mathbf{C}}^{-1}\bar{\mathbf{C}}\bar{\mathbf{x}}^e \end{aligned} \quad (4)$$

where $\hat{\mathbf{C}}$ is a $(E - V) \times (E - V)$ regular matrix. The similar relations hold for \mathbf{y}^e and \mathbf{z}^e , respectively. All the positions of nodes of a frame model can be determined by those of the independent nodes. The vector of the design variables of form generation is represented by $\mathbf{X} = (\bar{\mathbf{x}}^{eT}, \bar{\mathbf{y}}^{eT}, \bar{\mathbf{z}}^{eT})^T \in \mathbb{R}^{3V}$.

3. Procedure of form generation

In this section, a procedure is described for form generation of a developable and rigid-foldable polyhedral shape approximating the target surface, which is divided into triangular facets.

When a polyhedron can be developed to a plane, the Gaussian curvature at each interior vertex should be equal to zero. This condition is called *developability condition* in this paper. The Gaussian curvature at each interior vertex of the polyhedron is defined as the angle defect [22], i.e., the difference between 2π and the sum of angles between the adjacent edges connected to the interior vertex.

If rigid origami consists of only triangular facets, the DOF is often too large for practical use. Thus, some crease lines are fixed (removed) to reduce the DOF, and the pairs of adjacent facets connected to the fixed crease lines are integrated into flat facets. The condition that the polyhedron should satisfy to ensure the flatness of the n -gonal facets ($n > 3$) is called *flatness condition* in this paper.

The k th angle between the adjacent crease lines connected to vertex i is represented by $\theta_{i,k}$ ($i = 1, \dots, V$, $k = 1, \dots, f_i$) where f_i is the number of crease lines connected to vertex i . The unit normal vectors of the adjacent facets connected to edge j are denoted by $\mathbf{n}_{j,1} \in \mathbb{R}^3$ and $\mathbf{n}_{j,2} \in \mathbb{R}^3$ ($j = 1, \dots, E$), respectively. Let V_{in} and E_{fix} denote the sets of indices of interior vertices and the crease lines to be fixed, respectively. The following equation holds for a polyhedron which satisfies both the developability condition and the flatness condition [19, 20, 21]:

$$F(\mathbf{X}) = F_1(\mathbf{X}) + F_2(\mathbf{X}) = 0 \quad (5)$$

$$F_1(\mathbf{X}) = \sum_{i \in V_{\text{in}}} \left\{ 2\pi - \sum_{j=1}^{f_i} \theta_{i,k}(\mathbf{X}) \right\}^2$$

$$F_2(\mathbf{X}) = \sum_{j \in E_{\text{fix}}} \|\mathbf{n}_{j,1}(\mathbf{X}) \times \mathbf{n}_{j,2}(\mathbf{X})\|^2$$

Since it is difficult to analytically determine the polyhedral shape satisfying Eq. (5), a solution is obtained by solving the optimization problem to

minimize the non-negative function $F(\mathbf{X})$. When $F(\mathbf{X})$ converges to zero, the optimal shape satisfies the developability and flatness conditions. In this study, the z -coordinate of the target surface is represented as a function of the (x, y) coordinates as $z = f(x, y)$. Therefore, the error of the polyhedral surface from the target surface is measured by the difference between the z -coordinates of the vertices and the surface with the same (x, y) -coordinates. In addition, it is assumed that the surface does not have any hole for simplicity, and the projected shapes of the target surface and the polyhedron onto xy -plane are assumed to exist in a rectangular region. The difference between z -coordinates of vertex i and its projected point onto the target surface in z -direction is denoted by $\Delta z_i^v(\mathbf{X})$ ($i = 1, \dots, V$). The approximation accuracy is ensured by introducing the upper-bound constraint on the absolute value of Δz_i^v . To avoid an excessively acute triangular facet, the upper bound θ_{\max} and lower bound θ_{\min} are assigned for $\theta_{i,k}(\mathbf{X})$. Let χ denote the set of \mathbf{X} satisfying the conditions on the shape of the polyhedron. The optimization problem to obtain a developable polyhedron whose vertices are within a specified distance in the z direction from a given target surface, which is expressed as a height over the xy -plane, is formulated as follows as a nonlinear programming (NLP) problem:

$$\begin{cases} \min_{\mathbf{X}} & F(\mathbf{X}) = F_1(\mathbf{X}) + F_2(\mathbf{X}) \\ \text{s.t.} & |\Delta z_i^v(\mathbf{X})| \leq \Delta \bar{z}^v \quad (i = 1, \dots, V) \\ & \theta_{\min} \leq \theta_{i,k}(\mathbf{X}) \leq \theta_{\max} \quad (i = 1, \dots, V, k = 1, \dots, f_i) \\ & \mathbf{X} \in \chi \end{cases} \quad (6)$$

χ is set according to each problem. In this paper, the projected boundaries of the polyhedron onto xy -plane is fixed at its original shape, and accordingly, the vertices at the corners of the polyhedron are fixed at their original position. Since the projected shape of the polyhedron is rectangular, vertex i on the j th projected boundary edge should be on the specified plane. Let x_i^v and y_i^v represent the x - and y -coordinates of vertex i , and it is on the plane defined as $\beta_{1,j}x + \beta_{2,j}y + \beta_{3,j} = 0$ ($j = 1, \dots, 4$) using specified coefficients $\beta_{1,j}, \beta_{2,j}, \beta_{3,j}$. Then, x_i^v and y_i^v satisfy the following equation:

$$\beta_{1,j}x_i^v + \beta_{2,j}y_i^v + \beta_{3,j} = 0 \quad (i \in V_{\text{ex},j}, j = 1, \dots, 4) \quad (7)$$

where $V_{\text{ex},j}$ represents the set of vertices which are on the j th boundary edge ($j = 1, \dots, 4$). Defining z_i^v and \bar{z}_i^v as the z -coordinates of vertex i and its initial value, respectively, z_i^v of the corner vertex satisfy the following equation since the corner vertices are fixed:

$$z_i^v - \bar{z}_i^v = 0 \quad (i \in V_c) \quad (8)$$

where V_c represents the set of vertices which are at the corner of the polyhedron. The symmetry of the polyhedron also should be considered if the target surface and its triangulation have the symmetry property. Let Σ represent the set of pairs of vertices $\{i, i'\}$ which are located symmetrically. Assuming that the plane of symmetry of vertices $\{i, i'\} \in \Sigma$ is represented by $\gamma_{1,\{i,i'\}}x + \gamma_{2,\{i,i'\}}y + \gamma_{3,\{i,i'\}}z = 0$, the coordinates of vertices i and i' satisfy the following equation:

$$\begin{pmatrix} x_i^v - x_{i'}^v \\ y_i^v - y_{i'}^v \\ z_i^v - z_{i'}^v \end{pmatrix} = \frac{2(\gamma_{1,\{i,i'\}}x_i^v + \gamma_{2,\{i,i'\}}y_i^v + \gamma_{3,\{i,i'\}}z_i^v)}{\gamma_{1,\{i,i'\}}^2 + \gamma_{2,\{i,i'\}}^2} \begin{pmatrix} \gamma_{1,\{i,i'\}} \\ \gamma_{2,\{i,i'\}} \\ 0 \end{pmatrix} \quad (\{i, i'\} \in \Sigma) \quad (9)$$

Since the coordinates of vertices of the polyhedron can be expressed as the linear combination of the coordinates of nodes of the frame model [21], the linear equality constraints (7), (8), and (9) can be combined as follows:

$$\Gamma \mathbf{X} = \mathbf{0} \quad (10)$$

In the same way as the derivation of Eq. (4), the number of independent variables can be reduced by using Eq. (10). Let $\hat{\mathbf{X}}$ and $\bar{\mathbf{X}}$ represent the vectors of independent and dependent variables, respectively. $\hat{\mathbf{X}}$ can be calculated from $\bar{\mathbf{X}}$ as

$$\begin{aligned} [\hat{\Gamma} \quad \bar{\Gamma}] \begin{pmatrix} \hat{\mathbf{X}} \\ \bar{\mathbf{X}} \end{pmatrix} &= \hat{\Gamma} \hat{\mathbf{X}} + \bar{\Gamma} \bar{\mathbf{X}} = \mathbf{0} \\ \Rightarrow \hat{\mathbf{X}} &= -\hat{\Gamma}^{-1} \bar{\Gamma} \bar{\mathbf{X}} \end{aligned} \quad (11)$$

In Section 6, the number of variables are reduced by Eq. (11)

In addition, χ can include the nonlinear equality constraints or the inequality constraints. For example, the upper bound of the folding angle can be assigned to restrict the shape of the polyhedron. The folding angle of crease line j ($j \in E_{\text{free}}$) is denoted by $\rho_j(\mathbf{X})$ where E_{free} is the set of indices of crease lines that are not fixed. The absolute value of $\rho_j(\mathbf{X})$ is defined as follows:

$$|\rho_j(\mathbf{X})| = \arccos \{ \mathbf{n}_{j,1}(\mathbf{X}) \cdot \mathbf{n}_{j,2}(\mathbf{X}) \} \quad (j \in E_{\text{free}})$$

Then, the constraints on the folding angle can be written as

$$|\rho_j(\mathbf{X})| \leq \bar{\rho} \quad (j \in E_{\text{free}}, 0 < \bar{\rho} < \pi) \quad (12)$$

Other constraints also can be added to χ to satisfy the demand on the optimized shape; however, the constraints should be assigned properly to obtain a feasible solution.

Remark 1 *It is possible to minimize a norm of coordinate differences under the constraints $F_1(\mathbf{X}) = 0$ and $F_2(\mathbf{X}) = 0$. However, in this case, the optimization process may terminate without finding a feasible solution. By contrast, the optimal objective value of the problem (6) may have a small positive value, and the optimal shape cannot always be developed to a plane without deformation of its facet. However, in view of engineering application, the deformation of the facet is negligibly small in most cases as demonstrated in the numerical examples. In this study, the optimization is regarded as successful when the optimal objective value is less than the small positive value F_{tol} , which is set empirically.*

The optimization problem (6) is solved sequentially by fixing crease lines to reduce the DOF of the deformation mechanism. Developable and rigid-foldable polyhedra which have different DOFs can be obtained as solutions of the optimization problem (6) with different numbers of fixed crease lines. The criteria for selecting the crease line to be fixed are proposed in Section 5. If some crease lines that are not fixed are locked, then an alternative crease line is to be selected. The procedure of form generation of developable and rigid-foldable polyhedra that have facets with more than three vertices and small DOFs is summarized as follows:

- Step 1. Triangulate the target surface, and assign the nodes and the elements of frame model.
- Step 2. Initialize the index set of fixed crease lines as $E_{\text{fix}} = \phi$, and empty the solution list.
- Step 3. Solve the problem (6) to obtain a developable polyhedron.
- Step 4. If the optimization is not converged or the optimal objective value is more than F_{tol} , then go to Step 7; otherwise, go to Step 5.
- Step 5. Evaluate the infinitesimal deformation mechanism of the obtained polyhedron using the method described in Section 4. If $\text{DOF} \geq 1$ and there is no locked crease line, add the solution to the solution list and

go to Step 6; if $\text{DOF} \geq 1$ and the locked crease line exists, go to Step 7; otherwise, go to Step 8.

- Step 6. Add the index of the crease line to be fixed to E_{fix} , in accordance with the criterion presented in Section 5, and return to Step 3.
- Step 7. If $E_{\text{fix}} = \phi$, no developable polyhedron is obtained and try the different crease pattern; otherwise, replace the index of the last fixed crease line in E_{fix} with index of another crease line.
- Step 8. Generate a development diagram of each obtained polyhedron in the solution list using the procedure described below, and evaluate the errors of the length of corresponding edges in the three-dimensional shape and the development diagram.
- Step 9. Carry out large-deformation analysis of each developable polyhedron in the solution list, and evaluate its finite rigid-foldability.

The initial shape for first solving the optimization problem in Step 3 in the form generation procedure is the triangulated target surface generated in Step 1. From the second optimization process, the initial shape is the polyhedron obtained in the previous optimization process, which has an optimal objective value less than F_{tol} and no locked crease line. Most of the optimal shapes obtained in Step 3 satisfy the developability and flatness conditions with small errors. However, the error may be sometimes too large, and we should confirm in Step 8 that the development diagram of the obtained polyhedron can be generated with good accuracy. Since the value of the objective function $F(\mathbf{X})$ in the problem (6) cannot be minimized exactly to 0, the optimal solution contains error in the flatness condition, and the developability of the polyhedron is evaluated by generating the development diagram instead of simply confirming that the value of $F(\mathbf{X})$ is small enough. According to the surface flattening method proposed by Wang et al. [30], the development diagram is generated by minimizing the sum of the squares of edge length errors between the three-dimensional shape and the development diagram. Let l_j and l_j^{d} denote the lengths of edge j ($j = 1, \dots, E$) in the three-dimensional shape and the development diagram, respectively. In addition, let F and \mathbf{n}_k ($k = 1, \dots, F$) denote the number of facets and the unit normal vector of facet k , respectively. The direction of \mathbf{n}_k is defined so that the relation $\mathbf{n}_k \cdot \mathbf{z} \geq 0$ is satisfied where $\mathbf{z} = (0, 0, 1)^{\text{T}}$, if all the facets do not overlap with each other and are not flipped. The vector of x - and y -coordinates of the independent nodes in the development diagram, denoted by $\mathbf{X}^{\text{d}} \in \mathbb{R}^{2V}$, is obtained by solving the

following optimization problem which minimizes the non-negative function $D(\mathbf{X}^d)$:

$$\left\{ \begin{array}{l} \min_{\mathbf{X}^d} \quad D(\mathbf{X}^d) = \frac{\sum_{j=1}^E \{l_j^d(\mathbf{X}^d) - l_j\}^2}{\sum_{j=1}^E l_j^2} \\ \text{s.t.} \quad \mathbf{n}_k(\mathbf{X}^d) \cdot \mathbf{z} \geq 0 \quad (k = 1, \dots, F) \\ \quad \quad \mathbf{X}^d \in \chi^d \end{array} \right. \quad (13)$$

where χ^d denotes the set of variables which satisfy the condition so that the position of the development diagram is determined uniquely. The initial guess of the problem (13) can be arbitrarily set under the condition that it has the same connectivity of edges as the three-dimensional shape and satisfies the constraints of the optimization problem. In this study, the projected shape of the three-dimensional shape onto xy -plane is the initial guess of the problem (13). In addition, although the optimal shape obtained in Step 3 satisfies the developability and flatness conditions, continuous development from the surface to a plane is not guaranteed without deformation of the facets. Thus, the large-deformation analysis is carried out in Step 9 to confirm the existence of a finite deformation mechanism using a general finite element analysis software. If the deformation of each facet throughout the process of the analysis is small enough, it can be concluded that the obtained polyhedron is rigid-foldable. When a locked crease line exists in the optimal shape, it cannot be deployed to a plane without deformation of its facets even if it satisfies the developability condition. In such a case, it is necessary to change the crease line to be fixed in Step 7 and solve the optimization problem again.

The truss model or the rotational hinge model can be applied to the proposed form generation process described above. However, if the truss model is used, some bar elements should be added to reduce the DOF, and adding the elements is more complicated than simply fixing (removing) the hinge of the frame model. On the other hand, if the rotational hinge model is used and the variables of the form generation process are the inner angles of triangles and the folding angles, the complicated constraints on the angles are necessary so that the shape of the polyhedron is appropriately represented by the angles.

4. Prediction of transition of deformation mechanism by fixing crease lines

In Sections 2 and 3, the geometrical properties of the frame model have been described and the optimization problem has been formulated using the geometrical variables. In the following Sections 4 and 5, the deformation mechanism of the frame model is investigated based on the mechanical formulations of stiffness and stability.

4.1. Derivation of the deformation mode

In this section, infinitesimal rigid-folding modes are investigated using the method for stability analysis and finding mechanism of partially rigid frames which have arbitrarily inclined hinges [27, 28]. The transition of the deformation mechanism of the frame model by fixing the crease lines is predicted in Section 4.2 based on the infinitesimal rigid-folding modes derived from the eigenvectors of the generalized stiffness matrix. The selection criteria of the crease lines to be fixed are defined in Section 5 which reflect the prediction of the transition of the deformation mechanism.

The number of elements, nodes, and hinges of the frame model are denoted by m , n , and h , respectively. The total number of fixed nodal displacement degrees of freedom including both the translation and rotation is denoted by s . Let $\mathbf{S}_N \in \mathbb{R}^{(6n-s) \times 6m}$ and $\mathbf{S}_R \in \mathbb{R}^{h \times 6m}$ represent the matrices for the equilibrium equations of a frame and the constraints of the moments around the rotation axes of hinges, respectively. In the range of infinitesimal deformation, a vector $\mathbf{e} \in \mathbb{R}^{6m}$ representing the deformations of frame elements can be described by $\mathbf{u} \in \mathbb{R}^{6n-s}$ representing the unconstraint nodal displacements and $\boldsymbol{\varphi} \in \mathbb{R}^h$ representing the hinge rotations as follows:

$$\mathbf{e} = \mathbf{S}_N^T \mathbf{u} + \mathbf{S}_R^T \boldsymbol{\varphi} \quad (14)$$

The detailed derivation of \mathbf{S}_N and \mathbf{S}_R is shown in Appendix A. The vectors \mathbf{u} and $\boldsymbol{\varphi}$ are combined into $\mathbf{v} \in \mathbb{R}^{6n-s+h}$, and the displacement vector \mathbf{v} should satisfy the following compatibility equations represented by $\mathbf{S} = [\mathbf{S}_N^T \ \mathbf{S}_R^T] \in \mathbb{R}^{6m \times (6n-s+h)}$ so that the deformation of each frame element is zero:

$$\mathbf{S}_N^T \mathbf{u} + \mathbf{S}_R^T \boldsymbol{\varphi} = [\mathbf{S}_N^T \ \mathbf{S}_R^T] \begin{pmatrix} \mathbf{u} \\ \boldsymbol{\varphi} \end{pmatrix} = \mathbf{S} \mathbf{v} = \mathbf{0} \quad (15)$$

The displacement vector \mathbf{v} satisfying Eq. (15) is expressed as a linear combination of the bases of $\ker(\mathbf{S})$ [31] and the dimension d of $\ker(\mathbf{S})$ is the number of kinematic indeterminacy. The bases of $\ker(\mathbf{S})$ are the right singular vectors

of \mathbf{S} corresponding to zero singular values. Defining $r = \text{rank}(\mathbf{S})$, the number of kinematic indeterminacy d is computed as

$$d = 6n - s + h - r \quad (16)$$

When the nodal displacements are appropriately constrained so that the rigid-body motions of the entire model are constrained and the hinge rotations are not constrained, $s = 6$ holds in the three-dimensional space, and d is equal to the DOF of the internal deformation of the frame model. Let $\boldsymbol{\eta}_1, \dots, \boldsymbol{\eta}_d \in \mathbb{R}^{6n-s+h}$ denote the right singular vectors of \mathbf{S} corresponding to zero singular values, which are normalized as $\|\boldsymbol{\eta}_i\| = 1$ ($i = 1, \dots, d$). Then, the arbitrary displacement which does not cause deformation of the frame element is expressed using $\mathbf{a} = (a_1, \dots, a_d)^T \in \mathbb{R}^d$ and $\mathbf{H} = [\boldsymbol{\eta}_1 \cdots \boldsymbol{\eta}_d] \in \mathbb{R}^{(6n-s+h) \times d}$ as follows:

$$\begin{aligned} \mathbf{v} &= a_1 \boldsymbol{\eta}_1 + \cdots + a_d \boldsymbol{\eta}_d \\ &= [\boldsymbol{\eta}_1 \quad \cdots \quad \boldsymbol{\eta}_d] \begin{pmatrix} a_1 \\ \vdots \\ a_d \end{pmatrix} \\ &\equiv \mathbf{H} \mathbf{a} \end{aligned} \quad (17)$$

The matrix \mathbf{H} is divided into two matrices $\mathbf{H}_u \in \mathbb{R}^{(6n-s) \times d}$ and $\mathbf{H}_\varphi \in \mathbb{R}^{h \times d}$ corresponding to the rows 1 to $6n-s$ and the rows $6n-s+1$ to $6n-s+h$ of \mathbf{H} . The arbitrary nodal displacement vector \mathbf{u} and the hinge rotation vector $\boldsymbol{\varphi}$ without deformation of the frame element are derived from Eq. (17) as follows:

$$\mathbf{u} = \mathbf{H}_u \mathbf{a}, \quad \boldsymbol{\varphi} = \mathbf{H}_\varphi \mathbf{a} \quad (18)$$

As described above, the deformation modes of rigid origami represented by the frame model are obtained by using the mechanism analysis method of the partially rigid frames. The displacement modes of the vertices and the folding angle variation modes of rigid origami can be easily and simultaneously obtained from the nodal displacement modes of the frame and the hinge rotation modes, respectively, whereas only one of them can be obtained using the truss model or the rotational hinge model.

In addition, the equilibrium equation of the frame model without deformation of its element is derived by assigning the fictitious rotational stiffness K_j ($j = 1, \dots, h$, $K_j \geq 0$) at hinge (crease line) j . The external load $\mathbf{P} \in \mathbb{R}^{6n-s}$ is applied to the unconstrained degrees of freedom of nodal displacement. Defining $\mathbf{K} \in \mathbb{R}^{h \times h}$ as the diagonal matrix in which j th diagonal element is K_j ,

the total potential energy Π of the frame without deformation of the frame element is formulated as follows using Eq. (18):

$$\begin{aligned}
\Pi &= \frac{1}{2} \boldsymbol{\varphi}^T \mathbf{K} \boldsymbol{\varphi} - \mathbf{P}^T \mathbf{u} \\
&= \frac{1}{2} \mathbf{a}^T \left(\mathbf{H}_\varphi^T \mathbf{K} \mathbf{H}_\varphi \right) \mathbf{a} - (\mathbf{H}_u \mathbf{P})^T \mathbf{a} \\
&\equiv \frac{1}{2} \mathbf{a}^T \tilde{\mathbf{K}} \mathbf{a} - \tilde{\mathbf{P}}^T \mathbf{a}
\end{aligned} \tag{19}$$

According to the stationary condition of Π with respect to \mathbf{a} , the equilibrium equation is derived as

$$\tilde{\mathbf{P}} = \tilde{\mathbf{K}} \mathbf{a} \tag{20}$$

In this study, $\tilde{\mathbf{P}}$, $\tilde{\mathbf{K}} \in \mathbb{R}^{d \times d}$, and \mathbf{a} are called *pseudo external load*, *pseudo stiffness matrix*, and *pseudo displacement*, respectively.

Remark 2 *In Section 5, the ratios of the eigenvalue derivatives and the components of the eigenmodes of the stiffness matrix are used to formulate the selection criteria of the crease line to be fixed. Therefore, the stiffnesses of the hinges may not necessarily be small; only their ratios are important.*

The i th eigenvalue and the corresponding eigenvector of pseudo stiffness matrix $\tilde{\mathbf{K}}$, denoted by λ_i and $\boldsymbol{\alpha}_i$ ($i = 1, \dots, d$), respectively, satisfy the following equation:

$$\tilde{\mathbf{K}} \boldsymbol{\alpha}_i = \lambda_i \boldsymbol{\alpha}_i \tag{21}$$

Thus, λ_i is the stiffness in the direction represented by the nodal displacement $\mathbf{u}_i = \mathbf{H}_u \boldsymbol{\alpha}_i$ and the hinge rotation $\boldsymbol{\varphi}_i = \mathbf{H}_\varphi \boldsymbol{\alpha}_i$. The eigenvector $\boldsymbol{\alpha}_i$ ($\|\boldsymbol{\alpha}_i\| = 1$, $i = 1, \dots, d$) is supposed to be the orthonormal basis of the d -dimensional vector space, and $\mathbf{A} \in \mathbb{R}^{d \times d}$ is the orthogonal matrix whose i th column is $\boldsymbol{\alpha}_i$. In the following, the $i \times i$ identity matrix is denoted by \mathbf{I}_i . Since \mathbf{H} satisfies $\mathbf{H}^T \mathbf{H} = \mathbf{I}_d$, the following equation holds:

$$(\mathbf{H}\mathbf{A})^T (\mathbf{H}\mathbf{A}) = \mathbf{A}^T \mathbf{H}^T \mathbf{H} \mathbf{A} = \mathbf{I}_d \tag{22}$$

Therefore, $\mathbf{H}\boldsymbol{\alpha}_i$ ($i = 1, \dots, d$) can be used as the orthogonal deformation mode of the frame model, whose norm is equal to one. The arbitrary hinge rotation $\boldsymbol{\varphi}$ without deformation of each frame element can be expressed using a coefficient vector $\mathbf{b} = (b_1, \dots, b_d)^T \in \mathbb{R}^d$ as

$$\begin{aligned}
\boldsymbol{\varphi} &= b_1 \mathbf{H}_\varphi \boldsymbol{\alpha}_1 + \cdots + b_d \mathbf{H}_\varphi \boldsymbol{\alpha}_d \\
&= b_1 \boldsymbol{\varphi}_1 + \cdots + b_d \boldsymbol{\varphi}_d \\
&= [\boldsymbol{\varphi}_1 \quad \cdots \quad \boldsymbol{\varphi}_d] \begin{pmatrix} b_1 \\ \vdots \\ b_d \end{pmatrix} \\
&\equiv \boldsymbol{\Phi} \mathbf{b}
\end{aligned} \tag{23}$$

On the other hand, since $\boldsymbol{\alpha}_i$ satisfies the following relationship derived from Eq. (21)

$$\boldsymbol{\alpha}_j^T \tilde{\mathbf{K}} \boldsymbol{\alpha}_i = \lambda_i \boldsymbol{\alpha}_j^T \boldsymbol{\alpha}_i = \begin{cases} 0 & (i \neq j) \\ \lambda_i & (i = j) \end{cases}$$

the following equation holds:

$$\begin{aligned}
\begin{bmatrix} \boldsymbol{\alpha}_1^T \\ \vdots \\ \boldsymbol{\alpha}_d^T \end{bmatrix} \tilde{\mathbf{K}} [\boldsymbol{\alpha}_1 \quad \cdots \quad \boldsymbol{\alpha}_d] &= \begin{bmatrix} \boldsymbol{\alpha}_1^T \tilde{\mathbf{K}} \boldsymbol{\alpha}_1 & \cdots & \boldsymbol{\alpha}_1^T \tilde{\mathbf{K}} \boldsymbol{\alpha}_d \\ \vdots & \ddots & \vdots \\ \boldsymbol{\alpha}_d^T \tilde{\mathbf{K}} \boldsymbol{\alpha}_1 & \cdots & \boldsymbol{\alpha}_d^T \tilde{\mathbf{K}} \boldsymbol{\alpha}_d \end{bmatrix} = \begin{bmatrix} \lambda_1 & & 0 \\ & \ddots & \\ 0 & & \lambda_d \end{bmatrix} \\
\Leftrightarrow \mathbf{A}^T \tilde{\mathbf{K}} \mathbf{A} &= \boldsymbol{\Lambda}
\end{aligned} \tag{24}$$

where $\boldsymbol{\Lambda} = \text{diag}(\lambda_1, \dots, \lambda_d)$. Substituting $\tilde{\mathbf{K}} = \mathbf{H}_\varphi^T \mathbf{K} \mathbf{H}_\varphi$, $\boldsymbol{\varphi}_i = \mathbf{H}_\varphi \boldsymbol{\alpha}_i$ and $\boldsymbol{\Phi} = \mathbf{H}_\varphi \mathbf{A}$ into Eq. (24), $\boldsymbol{\Phi} \in \mathbb{R}^{h \times d}$ satisfies

$$\begin{aligned}
\begin{bmatrix} \boldsymbol{\alpha}_1^T \tilde{\mathbf{K}} \boldsymbol{\alpha}_1 & \cdots & \boldsymbol{\alpha}_1^T \tilde{\mathbf{K}} \boldsymbol{\alpha}_d \\ \vdots & \ddots & \vdots \\ \boldsymbol{\alpha}_d^T \tilde{\mathbf{K}} \boldsymbol{\alpha}_1 & \cdots & \boldsymbol{\alpha}_d^T \tilde{\mathbf{K}} \boldsymbol{\alpha}_d \end{bmatrix} &= \begin{bmatrix} \boldsymbol{\varphi}_1^T \mathbf{K} \boldsymbol{\varphi}_1 & \cdots & \boldsymbol{\varphi}_1^T \mathbf{K} \boldsymbol{\varphi}_d \\ \vdots & \ddots & \vdots \\ \boldsymbol{\varphi}_d^T \mathbf{K} \boldsymbol{\varphi}_1 & \cdots & \boldsymbol{\varphi}_d^T \mathbf{K} \boldsymbol{\varphi}_d \end{bmatrix} = \begin{bmatrix} \lambda_1 & & 0 \\ & \ddots & \\ 0 & & \lambda_d \end{bmatrix} \\
\Leftrightarrow \boldsymbol{\Phi}^T \mathbf{K} \boldsymbol{\Phi} &= \boldsymbol{\Lambda}
\end{aligned} \tag{25}$$

4.2. Prediction of the existence of locked crease lines

In this section, transition of the deformation mechanism by fixing the crease lines is predicted based on the result of the analysis of infinitesimal mechanism. The deformation mechanism after fixing the crease line is evaluated by the deformation modes before fixing the crease line. To ensure validity of the estimation of the change of deformation mechanism, it should

be assumed that the change of the shape of the polyhedron is small enough. When a crease line is fixed, the DOF of the mechanism decreases by 1, which is modeled as a process of reducing the size of the pseudo stiffness matrix. The reduction of DOF is also simulated as a process of increasing one eigenvalue to infinity as the stiffness of a hinge is increased to infinity. Suppose the rotational stiffness of hinge j is increased to a moderately large value to simulate the process of fixing crease line j ($j \in E_{\text{free}}$). Let ΔK_j ($\Delta K_j \gg 0$) denote the increase of the rotational stiffness of hinge j . Then, $\mathbf{K}' = \mathbf{K} + \Delta \mathbf{K}_j$ represents the diagonal matrix whose elements are the rotational stiffness of the hinges after increasing the stiffness of hinge j , where \mathbf{K} is the diagonal matrix whose elements are the original rotational stiffness of hinges and $\Delta \mathbf{K}_j$ is the matrix whose (j, j) element is ΔK_j and the other elements are 0, respectively. Assuming that \mathbf{H}_φ is invariant under the small change of the shape of the polyhedron due to fixing the crease line, the pseudo stiffness matrix after increasing the stiffness is calculated as $\tilde{\mathbf{K}}' = \mathbf{H}_\varphi^T \mathbf{K}' \mathbf{H}_\varphi$. The following equation holds for $i, k = 1, \dots, d$:

$$\begin{aligned}
\frac{1}{\Delta K_j} \boldsymbol{\alpha}'_i{}^T \tilde{\mathbf{K}}' \boldsymbol{\alpha}'_k &= \frac{1}{\Delta K_j} \boldsymbol{\alpha}'_i{}^T \mathbf{H}_\varphi^T (\mathbf{K} + \Delta \mathbf{K}_j) \mathbf{H}_\varphi \boldsymbol{\alpha}'_k \\
\Leftrightarrow \frac{\lambda'_k}{\Delta K_j} \boldsymbol{\alpha}'_i{}^T \boldsymbol{\alpha}'_k &= \boldsymbol{\varphi}'_i{}^T \left\{ \frac{1}{\Delta K_j} (\mathbf{K} + \Delta \mathbf{K}_j) \right\} \boldsymbol{\varphi}'_k \\
\Leftrightarrow \frac{\lambda'_k}{\Delta K_j} \boldsymbol{\alpha}'_i{}^T \boldsymbol{\alpha}'_k &\simeq \boldsymbol{\varphi}'_i{}^T \left(\frac{1}{\Delta K_j} \Delta \mathbf{K}_j \right) \boldsymbol{\varphi}'_k = \varphi'_{ij} \varphi'_{kj} \\
\Leftrightarrow \varphi'_{ij} \varphi'_{kj} &\simeq \begin{cases} 0 & (i \neq k) \\ \frac{\lambda'_k}{\Delta K_j} & (i = k) \end{cases}
\end{aligned} \tag{26}$$

where λ'_i and $\boldsymbol{\alpha}'_i$ ($i = 1, \dots, d$) are the i th eigenvalue and the corresponding eigenvector of the pseudo stiffness matrix $\tilde{\mathbf{K}}'$ after increasing the rotational stiffness of hinge j , respectively, and φ'_{ij} is the j th element of $\boldsymbol{\varphi}'_i = \mathbf{H}_\varphi \boldsymbol{\alpha}'_i$. Since $\varphi'_{ij} \varphi'_{kj} \simeq 0$ holds for any combination of i and k which have different values, $\varphi'_{ij} \simeq 0$ ($i = 1, \dots, d$) holds except one mode, i.e., hinge j can rotate in only one mode. If φ'_{kj} is not close to 0, the k th eigenvalue can be represented as $\lambda'_k \simeq \Delta K_j \varphi'^2_{kj} \gg 0$ according to Eq. (26), and it leads to a extremely high stiffness of the frame in the direction $\boldsymbol{\varphi}'_k$. Therefore, hinge j becomes fixed as its rotational stiffness is increased to a moderately large value.

On the other hand, the change of eigenvalues and eigenvectors of the pseudo stiffness matrix $\tilde{\mathbf{K}}$ under the increment of the rotational stiffness of the hinge can be estimated by the derivatives of eigenvalues and eigenvectors

of $\tilde{\mathbf{K}}$ with respect to the rotational stiffness. Detail of the derivation is shown in Appendix B. Assuming that the i th eigenvalue λ_i ($i = 1, \dots, d$) is distinct, its derivative with respect to j th hinge's rotational stiffness K_j ($j = 1, \dots, h$) is expressed as follows:

$$\begin{aligned}
\frac{\partial \lambda_i}{\partial K_j} &= \boldsymbol{\alpha}_i^T \frac{\partial \tilde{\mathbf{K}}}{\partial K_j} \boldsymbol{\alpha}_i \\
&= \boldsymbol{\alpha}_i^T \mathbf{H}_\varphi^T \frac{\partial \mathbf{K}}{\partial K_j} \mathbf{H}_\varphi \boldsymbol{\alpha}_i \\
&= \boldsymbol{\varphi}_i^T \frac{\partial \mathbf{K}}{\partial K_j} \boldsymbol{\varphi}_i \\
&= \varphi_{ij}^2
\end{aligned} \tag{27}$$

where φ_{ij} is the j th element of $\boldsymbol{\varphi}_i$, which is the (j, i) element of $\boldsymbol{\Phi}$.

Remark 3 *Assumption of distinct eigenvalues is generally satisfied because the rotational stiffness at each hinge is fictitious and can be assigned arbitrarily to avoid repeated eigenvalues. If repeated eigenvalues exist due to symmetry properties of the polyhedron, small random variations may be given for the hinge stiffnesses without any effect on the criteria derived below.*

According to Eq. (27), at least one eigenvalue is increased as the rotational stiffness K_j is increased since there is no locked hinges before K_j is increased, and $\varphi_{ij} \neq 0$ holds for at least one mode. Thus, according to Eq. (26), if the rotational stiffness of hinge j is increased to a moderately large value, φ_{ij} ($i = 1, \dots, d$) becomes 0 except one mode, say mode i' corresponding to a large increase of the eigenvalue. In this respect, it is natural to select the hinge with the maximum sensitivity coefficient of eigenvalue $\partial \lambda_i / \partial K_j$ to efficiently reduce the DOF of the mechanism. However, for more detailed investigation, we need to consider the variation of eigenvectors.

The derivative of the i th eigenvector $\boldsymbol{\alpha}_i$ with respect to K_j corresponding to the distinct eigenvalue is calculated as follows [32]:

$$\frac{\partial \boldsymbol{\alpha}_i}{\partial K_j} = - \sum_{\substack{k=1 \\ k \neq i}}^d \frac{1}{\lambda_k - \lambda_i} \left(\boldsymbol{\alpha}_k^T \frac{\partial \tilde{\mathbf{K}}}{\partial K_j} \boldsymbol{\alpha}_i \right) \boldsymbol{\alpha}_k = - \sum_{\substack{k=1 \\ k \neq i}}^d \frac{1}{\lambda_k - \lambda_i} \varphi_{kj} \varphi_{ij} \boldsymbol{\alpha}_k \tag{28}$$

Using the relation $\boldsymbol{\varphi}_i = \mathbf{H}_\varphi \boldsymbol{\alpha}_i$, Eq. (28) is rewritten as

$$\frac{\partial \boldsymbol{\varphi}_i}{\partial K_j} = \mathbf{H}_\varphi \frac{\partial \boldsymbol{\alpha}_i}{\partial K_j} = -\varphi_{ij} \sum_{\substack{k=1 \\ k \neq i}}^d \frac{1}{\lambda_k - \lambda_i} \varphi_{kj} \boldsymbol{\varphi}_k \tag{29}$$

From Eqs. (27) and (29), and using the relation $\partial\lambda_i/\partial K_j \geq 0$ that holds for any i ($i = 1, \dots, d$), the derivatives of the distinct eigenvalue and the corresponding eigenvector satisfy the following equation:

$$\frac{\partial \boldsymbol{\varphi}_i}{\partial K_j} = -\text{sgn}(\varphi_{ij}) \sqrt{\frac{\partial \lambda_i}{\partial K_j}} \sum_{\substack{k=1 \\ k \neq i}}^d \frac{\text{sgn}(\varphi_{kj})}{\lambda_k - \lambda_i} \sqrt{\frac{\partial \lambda_k}{\partial K_j}} \boldsymbol{\varphi}_k \quad (30)$$

where $\text{sgn}(\varphi_{kj})$ and $\text{sgn}(\varphi_{ij})$ are the signs of φ_{kj} and φ_{ij} , respectively.

Suppose φ_{ij} ($i = 1, \dots, d$) becomes 0 as K_j is increased except mode i' corresponding to a large increase of the eigenvalue. In the case that hinge j' ($j' \neq j$) is locked, $\varphi_{ij'} = 0$ also holds except mode i' . If $\partial\lambda_i/\partial K_j$ ($i = 1, \dots, d$) have large values, then from Eq. (30) the absolute values of $\partial\varphi_{ij}/\partial K_j$ have large values, and the values of φ_{ij} ($i \neq i'$) rapidly converge to 0 as K_j is increased without drastically changing the values of $\varphi_{ij'}$ ($j' \neq j$) as demonstrated in the numerical examples. Therefore, in this case, hinge j can be fixed independently without locking other hinges. Furthermore, suppose hinge j is fixed and there exists hinge p ($p \neq j$) approximately satisfying $\boldsymbol{\Psi}_j \cdot \boldsymbol{\Psi}_p = 1$ where $\boldsymbol{\Psi}_j = (\psi_{j1}, \dots, \psi_{jd})^T$ represents the normalized j th row of $\boldsymbol{\Phi}$, whose i th element ψ_{ji} is defined as

$$\psi_{ji} = \frac{\varphi_{ij}}{\sqrt{\sum_{i=1}^d \varphi_{ij}^2}} \quad (31)$$

In other words, $\varphi_{ip} \simeq c\varphi_{ij}$ is satisfied for all modes $i = 1, \dots, d$ with a constant c . Then, from Eq. (30), $\partial\varphi_{ij}/\partial K_j \simeq c\partial\varphi_{ip}/\partial K_j$ is satisfied, and $\boldsymbol{\Psi}_j \cdot \boldsymbol{\Psi}_p \simeq 1$ or $\varphi_{ip} \simeq c\varphi_{ij}$ is always satisfied as K_j is increased to a moderately large value. Therefore, φ_{ip} ($i \neq i'$) converges to 0, if φ_{ij} ($i \neq i'$) converges to 0 as K_j is increased. Consequently, the following properties hold:

Properties of eigenmodes of stiffness matrix:

1. When hinge j with a large maximum eigenvalue derivative is fixed, it is unlikely that there exists a locked hinge among the unfixed hinges when the rotation of hinge j in the deformation mechanism is modified to 0 to reduce the DOF of the mechanism.
2. If hinge j is fixed and there exists hinge p ($p \neq j$) approximately satisfying $\boldsymbol{\Psi}_j \cdot \boldsymbol{\Psi}_p = 1$ or $\varphi_{ij} = c\varphi_{ip}$ for all $i = 1, \dots, d$, then hinge p is likely to be locked.

5. Selection criterion of the crease lines to be fixed

In this section, a criterion is introduced for the selection of crease lines to be fixed in Steps 6 and 7 of the form generation procedure described in Section 3. It is important to fix an appropriate crease line so that the objective function of the optimization problem (6) easily converges to zero and unfixed crease lines are not locked after fixing the crease line. Therefore, it is necessary to determine the crease lines to be fixed in consideration of both the shape of the polyhedron approximating the target surface and the possibility of existence of a locked crease line as discussed in Section 4.

The score of crease line $j \in E_{\text{free}}$ in terms of the shape of the polyhedron is denoted by S_j^{S} , which is defined by the folding angle ρ_j of crease line j as

$$S_j^{\text{S}} = \frac{|\rho_j|}{\sum_{j=1}^h |\rho_j|} \quad (32)$$

A small value of S_j^{S} leads to nearly parallel adjacent facets connected to crease line j , and consequently, a small shape change of the polyhedron after fixing crease line j . Thus, the objective function of problem (6) is likely to converge to zero when the crease line with the smallest score S_j^{S} is fixed.

On the other hand, the score S_j^{F} of crease line $j \in E_{\text{free}}$ is defined as follows using the eigenvalue derivatives of the pseudo stiffness matrix $\tilde{\mathbf{K}}$ with respect to the rotational stiffness K_j of crease line j :

$$S_j^{\text{F}} = \frac{\max_i \left(\frac{\partial \lambda_i}{\partial K_j} \right)}{\sum_{j=1}^h \max_i \left(\frac{\partial \lambda_i}{\partial K_j} \right)} \quad (33)$$

Based on Property 1 in Section 4, a larger value of S_j^{F} leads to a smaller possibility of locking a crease line that is not fixed. Furthermore, if all the eigenvalues of $\tilde{\mathbf{K}}$ are distinct, S_j^{F} can be expressed by substituting Eq. (27) into Eq. (33) as

$$S_j^{\text{F}} = \frac{\max_i \left(\varphi_{ij}^2 \right)}{\sum_{j=1}^h \max_i \left(\varphi_{ij}^2 \right)} \quad (34)$$

The numerator of S_j^{F} indicates how dominant the rotation of crease line j is among the rotations in all the deformation modes. Because φ_{ij} is the j th component of $\boldsymbol{\varphi}_i$, a large value of S_j^{F} suggests that crease line j can rotate independently, and there is a small possibility of locking an unfixed crease line.

Therefore, S_j^F can be used to define the score of crease line j in terms of the deformation mechanism. However, since the matrix Φ , whose (j, i) element is φ_{ij} , is not normalized with respect to both rows and columns, simply comparing the values of φ_{ij}^2 may be insufficient to determine the crease line to be fixed. Here, Φ is normalized with respect to its columns based on Eq. (25). Assuming $K_1 = \dots = K_h = K$; i.e. $\mathbf{K} = K\mathbf{I}_h$, the following equation holds for $k, l = 1, \dots, d$:

$$\boldsymbol{\varphi}_l^T \boldsymbol{\varphi}_k = \begin{cases} 0 & (k \neq l) \\ \frac{\lambda_k}{K} & (k = l) \end{cases}$$

Hence, defining $\hat{\Phi} \in \mathbb{R}^{h \times d}$ as the matrix whose i th column is the i th column of Φ multiplied by $\sqrt{K/\lambda_i}$, $\hat{\Phi}$ satisfies the following equation and it is normalized with respect to its columns:

$$\begin{aligned} \hat{\Phi}^T \hat{\Phi} &= \begin{bmatrix} \frac{K}{\lambda_1} \boldsymbol{\varphi}_1^T \boldsymbol{\varphi}_1 & \cdots & 0 \\ \vdots & \ddots & \vdots \\ 0 & \cdots & \frac{K}{\lambda_d} \boldsymbol{\varphi}_d^T \boldsymbol{\varphi}_d \end{bmatrix} \\ &= \mathbf{I}_d \end{aligned} \quad (35)$$

Instead of S_j^F in Eq. (33), another score \hat{S}_j^F of crease line j can be defined by the (j, i) element $\hat{\varphi}_{ij}$ of $\hat{\Phi}$ as follows:

$$\hat{S}_j^F = \frac{\max_i (\hat{\varphi}_{ij}^2)}{\sum_{j=1}^h \max_i (\hat{\varphi}_{ij}^2)} \quad (36)$$

To incorporate both of the change of the shape and the change of the deformation mechanism of the polyhedron after fixing a crease line, the following two different scores S_j and \hat{S}_j of crease line $j \in E_{\text{free}}$ are used as the criteria to determine the crease line to be fixed in the process of form generation described in Section 3:

$$S_j = \frac{S_j^S}{S_j^F} \quad (37)$$

$$\hat{S}_j = \frac{S_j^S}{\hat{S}_j^F} \quad (38)$$

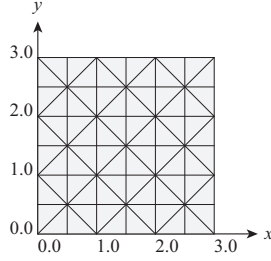


Figure 5: Crease pattern 1

The crease line that has the lowest score is fixed sequentially. Multiple crease lines can also be fixed simultaneously if the polyhedron has a symmetry property. Let j_1, \dots, j_h denote the indices of crease lines in ascending order of S_j or \hat{S}_j , i.e., $S_{j_1} \leq \dots \leq S_{j_h}$ or $\hat{S}_{j_1} \leq \dots \leq \hat{S}_{j_h}$ holds. When h_{fix} ($1 \leq h_{\text{fix}} \leq h$) crease lines are simultaneously fixed, h_{fix} indices $j_1, \dots, j_{h_{\text{fix}}}$ are added to E_{fix} in Step 6 of the form generation procedure. If there is a locked crease line in the optimal shape obtained in the subsequent optimization process, $j_1, \dots, j_{h_{\text{fix}}} \in E_{\text{fix}}$ are replaced with $j_{h_{\text{fix}}+1}, \dots, j_{h_{\text{fix}}+h'_{\text{fix}}}$ where h'_{fix} is the number of indices added to E_{fix} in Step 7.

6. Numerical examples

6.1. Model description and parameter settings

In Sections 6.2, 6.3 and 6.4, the examples of form generation are shown for the rigid-foldable origami models with two different crease patterns shown in Figs. 5 and 6. The performances of the selection criteria of the crease line to be fixed introduced in Section 5 are evaluated by comparing the form generation results by using S_j , \hat{S}_j , S_j^S , and randomly selecting the crease line to be fixed. The results are discussed statistically by randomly generating 100 target surfaces for each pattern; i.e., in total, 200 cases of form generation are performed in this section. Furthermore, the examples which have dome and hyperbolic paraboloid (HP) shapes, respectively, with more complex crease patterns are shown in Sections 6.5 and 6.6.

A 3×3 Bézier surface [33] is used as the target surface. The x - and y -coordinates of its control points are located at uniform intervals as shown in Fig. 7. The projected shape of the target surface onto xy -plane is a 3×3 m square, and the z -coordinates are randomly set in the range between 0 and 3 m.

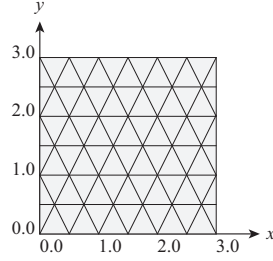


Figure 6: Crease pattern 2

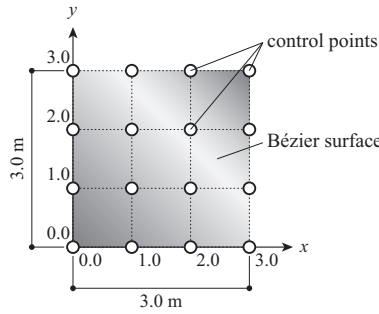


Figure 7: Control points of Bézier surface

The parameters for the optimization problem (6) are assigned as $\Delta\bar{z}^u = 0.30$ m, $\theta_{\min} = \pi/6$ and $\theta_{\max} = 2\pi/3$. In Sections 6.2, 6.3 and 6.4, the constraints on the projected boundaries and the corner vertices of the polyhedron represented by Eq. (7) and Eq. (8) are considered. However, the symmetry condition represented by Eq. (9) and the constraints on the folding angles represented by Eq. (12) are not assigned. The number of variables in the optimization is reduced by Eq. (11). The tolerance F_{tol} of $F(\mathbf{X})$ in the problem (6) is 1.0×10^{-7} . The rotation stiffness of the hinges are randomly set in the range between $1.0 \times 10^{-3} - 0.5 \times 10^{-6}$ and $1.0 \times 10^{-3} + 0.5 \times 10^{-6}$ (Nm) to avoid the existence of repeated eigenvalues. The optimization problem (6) is solved using SLSQP (Sequential Least Squares Programming) available in Python library SciPy. Infinitesimal deformation modes are obtained by SVD in Python library Numpy. Abaqus 2016 [34] is used in large deformation analysis. The frame model is constructed with three-dimensional beam elements which have cylindrical cross sections of 20 mm diameter and 1 mm wall thickness. Their Young's modulus and Poisson's ratio are 200 GPa and 0.3, respectively. Hinge connectors representing the revolute joints are used for modeling the crease lines. Although the rotation stiffness of the hinge

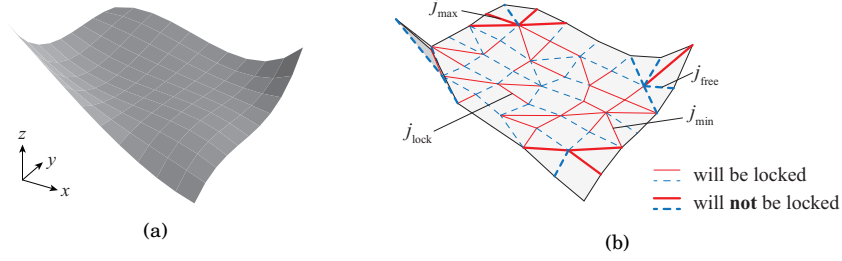


Figure 8: Example of the optimal shape including the crease lines which will be locked: (a) target surface; (b) optimal shape before fixing crease line j_{fix}

connector is not necessary to the large-deformation analysis, the small rotation stiffness 1.0×10^{-3} (Nm) is introduced to each hinge connector to stabilize the analysis. To deploy the polyhedron onto xy -plane, forced displacement in z -direction is applied at each node on the facet. The elongation Δl_j of edge j ($j = 1, \dots, E$) and the error of the dihedral angle $\Delta \rho_j^{\text{fix}}$ between the facets connected to the fixed crease line $j \in E_{\text{fix}}$ is calculated from the nodal displacements of the frame model. If both Δl_j for all the edges and $\Delta \rho_j^{\text{fix}}$ for all the fixed crease lines are acceptably small in view of engineering application, the obtained polyhedral surface is regarded as developable and rigid-foldable. Computation is carried out on a PC with Intel(R) Xeon(R) E5-1620 v3 CPU 3.50 GHz, 24.0 GB RAM, and four cores.

6.2. Numerical example including the locked crease lines

This subsection shows an example of optimization process where some crease lines that are not fixed will be locked after fixing a crease line. The transition of the deformation mechanism is investigated by increasing the rotational stiffness of the hinge (crease line) which has the maximum or the minimum value of S_j^F defined by Eq. (33). The target surface is shown in Fig. 8(a) and the crease pattern 1 shown in Fig. 5 is applied for the initial shape. The optimal shape is shown in Fig. 8(b) which has a 7-DOF mechanism, and none of its crease lines is currently locked.

The values of S_j^F and \hat{S}_j^F at crease line j_{max} are the largest, respectively, among the crease lines, and those at crease line j_{min} are the smallest. Therefore, the transition of the rotation modes are investigated by increasing the rotation stiffness of crease lines j_{max} and j_{min} , respectively, to make one eigenvalue of the pseudo stiffness matrix extremely larger than the other six eigenvalues. The shape of the polyhedron is fixed in this investigation. The elements φ_{ij} ($i = 1, \dots, 7$) of the seven rotation modes of crease lines j_{max} and j_{min} before increasing the rotational stiffness of crease line j_{max} or j_{min} are

Table 1: Eigenvalues and rotation modes (φ_{ij} : multiplied by 10^3)

i	λ_i	$\varphi_{ij_{\min}}$	$\varphi_{ij_{\max}}$	$\varphi_{ij_{\text{lock}}}$	$\varphi_{ij_{\text{free}}}$
1	3.79×10^{-6}	-0.31	-0.71	-0.61	2.50
2	1.08×10^{-4}	4.22	-5.05	8.30	-65.96
3	1.24×10^{-4}	2.14	-18.28	4.20	20.48
4	1.37×10^{-4}	-0.91	42.04	-1.79	5.41
5	2.40×10^{-4}	10.52	6.27	20.69	-79.75
6	3.13×10^{-4}	-1.01	6.81	-1.98	-315.03
7	4.11×10^{-4}	2.33	481.06	4.59	-6.94

shown in Table 1. The rotation modes of crease lines j_{locked} and j_{free} shown in Fig. 8(b), which are locked and not locked after increasing the rotational stiffness of crease line j_{\min} to a large value, are also listed in Table 1. Tables 2 and 3 show the rotation modes of the crease lines when the rotational stiffnesses $K_{j_{\max}}$ and $K_{j_{\min}}$ are multiplied by 10^{14} , respectively. As seen from these tables, if the rotational stiffness of one crease line is significantly increased, the largest eigenvalue becomes extremely larger than the others, and the crease line whose rotational stiffness is increased can rotate only in the rotation mode corresponding to the largest eigenvalue, i.e. it is fixed. The result in Table 2 indicates that crease line j_{\max} is fixed to reduce the DOF to six without locking other crease lines. On the other hand, when crease line j_{\min} is fixed, crease line j_{lock} is locked, because it does not have non-zero component except in the rotation mode corresponding to the largest eigenvalue as shown in Table 3. In this example, the crease lines indicated by the thin lines in Fig. 8(b) are locked when $K_{j_{\min}}$ is multiplied by 10^{14} . Comparing the results in Tables 2 and 3, it can be confirmed that the crease lines that are not fixed are locked as $K_{j_{\min}}$ corresponding to the smallest values of S_j^F and \hat{S}_j^F is increased to the moderately large value, whereas no crease line is locked as $K_{j_{\max}}$ corresponding to the largest values of S_j^F and \hat{S}_j^F is increased to moderately large value. From Table 1, the inner products of $\boldsymbol{\psi}_{j_{\min}}$ and $\boldsymbol{\psi}_j$ ($j \in \{j_{\text{lock}}, j_{\text{free}}\}$) are calculated as 1.00 and -0.20, respectively. Therefore, if the values of S_j^F and \hat{S}_j^F of the crease line to be fixed are small, the crease line j_{lock} whose corresponding $\boldsymbol{\psi}_{j_{\text{lock}}}$ is almost parallel to $\boldsymbol{\psi}_j$ of the crease line to be fixed is likely to be locked as described in Property 2 in Section 4.

6.3. Crease pattern 1

The initial shape of the form generation in this subsection has the crease pattern 1 which is shown in Fig. 5. The DOF of the optimal shape is 21 when

Table 2: Eigenvalues and rotation modes when $K_{j_{\max}}$ is multiplied by 10^{14} (φ_{ij} : multiplied by 10^3)

i	λ_i	$\varphi_{ij_{\min}}$	$\varphi_{ij_{\max}}$	$\varphi_{ij_{\text{lock}}}$	$\varphi_{ij_{\text{free}}}$
1	4.14×10^{-6}	-0.31	0.00	-0.62	2.44
2	1.07×10^{-4}	4.34	0.00	8.53	-64.42
3	1.22×10^{-4}	2.27	0.00	4.46	19.88
4	1.38×10^{-4}	1.42	0.00	2.79	-7.73
5	2.40×10^{-4}	10.46	0.00	20.58	-79.83
6	3.14×10^{-4}	1.06	0.00	2.08	314.78
7	2.34×10^{10}	2.24	483.36	4.40	-12.00

Table 3: Eigenvalues and rotation modes when $K_{j_{\min}}$ is multiplied by 10^{14} (φ_{ij} : multiplied by 10^3)

i	λ_i	$\varphi_{ij_{\min}}$	$\varphi_{ij_{\max}}$	$\varphi_{ij_{\text{lock}}}$	$\varphi_{ij_{\text{free}}}$
1	3.92×10^{-6}	0.00	0.25	0.00	0.34
2	1.18×10^{-4}	0.00	3.84	0.00	-52.18
3	1.32×10^{-4}	0.00	2.23	0.00	-3.15
4	1.40×10^{-4}	0.00	55.36	0.00	2.61
5	3.13×10^{-4}	0.00	-0.24	0.00	-321.57
6	4.04×10^{-4}	0.00	-471.39	0.00	-0.39
7	1.40×10^7	11.85	91.35	23.31	-65.63

Table 4: Numbers of vertices, edges, facets, and independent variables

Section	Vertex	Edge	Facet	Independent variable
6.2	49	120	72	115
6.3	52	117	78	124
6.4, 6.5 (symmetric)	121	320	200	83
6.4, 6.5 (asymmetric)	121	320	200	315

Table 5: Average results of form generation for crease pattern 1

	N_{reduce}	N_{lock}	N_{exceed}	$F(\mathbf{X})$
S_j	20.00	1.13	0.04	1.18×10^{-9}
\hat{S}_j	20.00	0.06	0.01	1.38×10^{-9}
S_j^S	19.97	24.94	0.03	2.19×10^{-9}
random	19.99	7.32	0.20	2.44×10^{-9}

the crease lines are not fixed. Form generation is carried out by sequentially solving optimization problems with increasing number of fixed crease lines. The numbers of vertices, edges, and facets of the polyhedron with triangular facets are summarized in Table 4. The numbers of independent variables in the optimization problem (6), which is 115 in this subsection, are also shown in Table 4. Let N_{reduce} , N_{lock} , and N_{exceed} denote the reduced DOFs from 21 in form generation process, the number of times any locked crease line exists, and the number of times the optimal objective value exceeds the tolerance, respectively. The 0-DOF optimal shape may be obtained in the final optimization cycle of the form generation procedure described in Section 3; however, it is not counted in N_{reduce} , N_{lock} , and N_{exceed} . Table 5 shows the average values of N_{reduce} , N_{lock} , and N_{exceed} among the results of form generation for 100 different target surfaces by using each selection criterion of the crease line to be fixed. The average values of $F(\mathbf{X})$ are also shown in Table 5. Although the average values of N_{reduce} are almost the same among the four selection criteria, the average value of N_{lock} is significantly reduced by using S_j or \hat{S}_j , and the latter has a slightly better performance. In addition, the value of $F(\mathbf{X})$ is also decreased by using S_j or \hat{S}_j . Therefore, the selection criteria S_j and \hat{S}_j improve both the accuracy and the efficiency of the form generation for various target surfaces when the crease pattern 1 is applied.

Fig. 10 shows the 1-DOF optimal shape for the target surface shown in Fig. 9 which is obtained by using \hat{S}_j as the selection criterion. The 20 crease lines of the initial triangulated polyhedron are fixed, and all the crease lines which are not fixed can rotate in the folding and unfolding process. The opti-

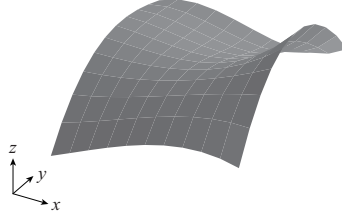


Figure 9: Target surface for the example in which crease pattern 1 is applied

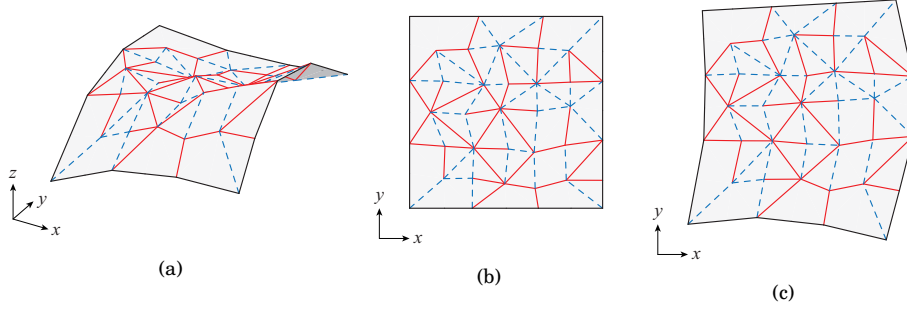


Figure 10: 1-DOF optimal shape for the target surface in Fig. 9 and the crease pattern 1 in Fig. 5: (a) isometric projection; (b) projection onto xy -plane; (c) development diagram

mal objective value of $F(\mathbf{X})$ of this solution is 1.02×10^{-8} , which is sufficiently small. The value of $D(\mathbf{X}^d)$ in Eq. (13) is 3.45×10^{-10} , and the development diagram of the obtained polyhedron can be generated with good accuracy as shown in Fig. 10(c). The average values of $|\Delta l_j|$ ($j = 1, \dots, E$) and $|\Delta \rho_j^{\text{fix}}|$ ($j \in E_{\text{fix}}$) throughout the process of large-deformation analysis are 0.25 mm and 0.018 deg., respectively. They are small enough and it can be concluded that the obtained polyhedron shown in Fig. 10 can be developed to a plane continuously in rigid-folding motion. In the form generation procedure for the target surface shown in Fig. 9, the optimization problem 6 is solved 22 times, and all the optimal objective values are less than $F_{\text{tol}} = 1.0 \times 10^{-7}$, whose average value is 1.31×10^{-9} . All the optimal shapes do not contain any locked crease line except for the final optimal shape whose 21 crease lines are fixed and the DOF is equal to zero. Therefore, N_{reduce} , N_{lock} , and N_{exceed} are 20, 0, and 0, respectively, in this example.

The average computation times of the 20 solutions for solving the optimization problems (6) and (13), performing the large deformation analysis, and selecting the crease lines to be fixed are 72.4 sec., 3.31 sec., 37.0 sec., and 0.0113 sec., respectively. The total computation time to obtain the 20 solutions is 2367 sec..

Table 6: Average results of form generation for crease pattern 2

	N_{reduce}	N_{lock}	N_{exceed}	$F(\mathbf{X})$
S_j	19.96	2.74	0.00	1.17×10^{-9}
\hat{S}_j	19.97	0.92	0.02	1.28×10^{-9}
S_j^S	19.73	28.60	0.14	1.93×10^{-9}
random	19.81	13.32	0.19	4.41×10^{-9}

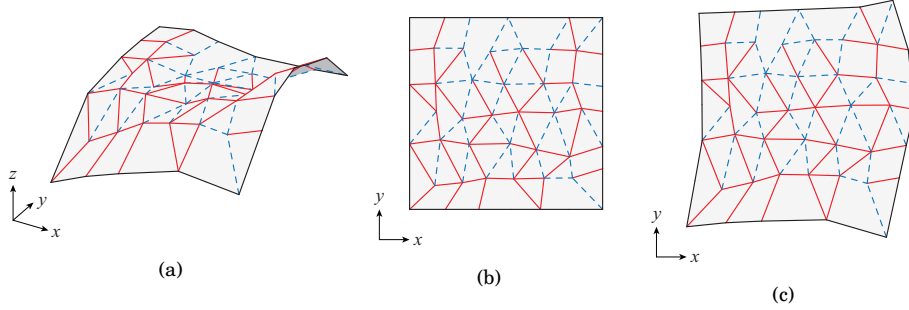


Figure 11: 1-DOF optimal shape for the target surface in Fig. 9 and the crease pattern 2 in Fig. 6: (a) isometric projection; (b) projection onto xy -plane; (c) development diagram

6.4. Crease pattern 2

The initial shape of the form generation in this subsection has the crease pattern 2 which is shown in Fig. 6. The DOF of the optimal shape obtained by the initial triangulated polyhedron without fixed crease lines is 21. As shown in Table 4, the number of independent variables in the optimization problem (6) is 124. The average values of N_{reduce} , N_{lock} , N_{exceed} , and $F(\mathbf{X})$ are summarized in Table 6. As shown in Table 6, both the accuracy and the efficiency of the form generation is improved by using the selection criterion S_j or \hat{S}_j also when the crease pattern 2 is applied, which means that the criterion S_j^S based on the geometrical property only is not appropriate, and the mechanical properties are necessary to be considered for an appropriate determination of the crease line to be fixed. Note that \hat{S}_j has a slightly better performance than S_j in view of N_{lock} also for pattern 2.

The 1-DOF optimal shape approximating the surface in Fig. 9 is shown in Fig. 11 which is obtained by using the criterion \hat{S}_j . The values of $F(\mathbf{X})$ and $D(\mathbf{X}^d)$ are 2.24×10^{-9} and 3.45×10^{-10} , respectively. In addition, the average values of $|\Delta l_j|$ ($j = 1, \dots, E$) and $|\Delta \rho_j^{\text{fix}}|$ ($j \in E_{\text{fix}}$) throughout the process of large-deformation analysis are calculated as 0.21 mm and 0.009 deg., respectively. Therefore, the obtained polyhedron shown in Fig. 11 can be regarded



Figure 12: Target dome surface with positive gaussian curvature

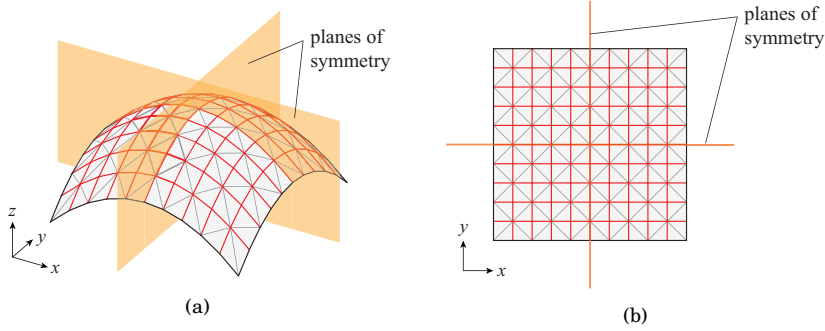


Figure 13: Initial triangulation and planes of symmetry: (a) isometric projection; (b) projection onto xy -plane

as developable and rigid-foldable. In this form generation example, N_{reduce} , N_{lock} , and N_{exceed} are 20, 0, and 0, respectively, and the average optimal objective value is 2.69×10^{-10} .

The average computation times of the 20 solutions for solving the optimization problems (6) and (13), performing the large deformation analysis, and selecting the crease lines to be fixed are 79.3 sec., 3.83 sec., 38.6 sec., and 0.00840 sec., respectively. The total computation time to obtain the 20 solutions is 2558 sec..

6.5. Dome surface

In this subsection, the target surface is the dome surface as shown in Fig. 12 whose height is 1.5 m and the projected shape onto xy -plane is a 3×3 m square. In addition to the constraints on the boundary shape of the polyhedron, the symmetry property is considered in the constraints of optimization problem (6). The triangulation pattern and the planes of symmetry are shown in Fig. 13. S_j defined by Eq. (37) is used as the selection criterion of the crease line to be fixed in this subsection. The DOF of the mechanism of the initial shape is 37, and it is reduced by fixing the crease lines which are located at symmetrical positions. As shown in Table 4, the number of independent

Table 7: Results of form generation for the dome surface

	symmetry	asymmetry
N_{lock}	1	1
N_{exceed}	0	0
Min. DOF	3	1
No. of opt.	11	38
Ave. $F(\mathbf{X})$	1.42×10^{-9}	2.78×10^{-9}
Ave. $D(\mathbf{X}^{\text{d}})$	1.13×10^{-10}	5.89×10^{-10}
Ave. $ \Delta l_j $ [mm]	0.793	1.09
Ave. $ \Delta \rho_j^{\text{fix}} $ [deg.]	6.59×10^{-2}	9.63×10^{-2}

variables in the optimization problem (6) in this subsection is 83 when the symmetry condition is considered or 315 when the symmetry condition is not considered. The results of the form generation with and without the symmetry conditions, respectively, are shown in Table 7. The optimization problem (6) is solved 11 times when the symmetry is considered and 38 times when the symmetry is not considered. In both cases, one optimal shape contains the locked crease lines. Although the average values of objective functions in problem (6) and (13) and the deformation of the polyhedron in the process of large deformation analysis are reduced by considering the symmetry condition, the minimal DOF of the mechanism of the symmetric model is 3, which is larger than that of the asymmetric model. Since two or four crease lines are simultaneously fixed and the DOF is reduced by two or four, it is difficult to obtain the single-DOF solution when the symmetry condition is considered.

Fig. 14 shows the symmetric 3-DOF optimal shape, where the 34 crease lines of the initial triangulated polyhedron are fixed, and all the crease lines which are not fixed can rotate in the folding and unfolding process. The optimal objective values of $F(\mathbf{X})$ and $D(\mathbf{X}^{\text{d}})$ of this solution are 1.29×10^{-10} and 4.70×10^{-11} , respectively, and the development diagram can be generated with good accuracy as shown in Fig. 14(c). The average values of $|\Delta l_j|$ ($j = 1, \dots, E$) and $|\Delta \rho_j^{\text{fix}}|$ ($j \in E_{\text{fix}}$) throughout the process of large-deformation analysis are 1.83 mm and 0.213 deg., respectively. Therefore, it can be concluded that the optimal shape shown in Fig. 14 is developable to a plane with a small deformation.

When the symmetry is considered, the average computation times for solving the optimization problems (6) and (13), performing the large deformation analysis, and selecting the crease lines to be fixed are 202 sec., 1.91 sec., 46.4 sec., 0.964 sec., respectively. The total computation time to obtain

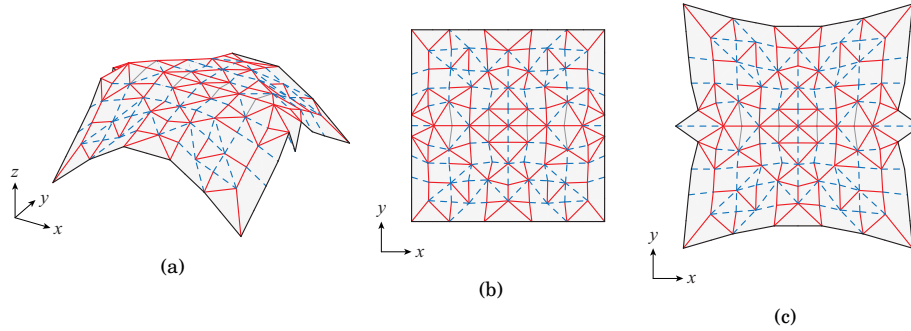


Figure 14: 3-DOF optimal shape for the target dome surface: (a) isometric projection; (b) projection onto xy -plane; (c) development diagram

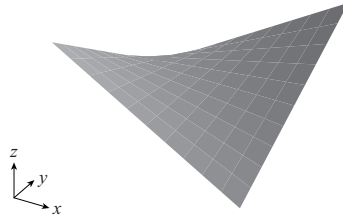


Figure 15: Target HP surface with negative gaussian curvature

the 10 solutions without locked crease lines is 2760 sec. including the time for generating one solution with locked crease lines. On the other hand, when the symmetry is not considered, the average computation times are 1015 sec., 20.3 sec., 52.7 sec., and 0.882 sec., respectively, and the total computation time to obtain the 37 solutions is 42768 sec.. The computation cost is considerably reduced by considering the symmetry and reducing the number of independent variables.

6.6. HP surface

In this subsection, the target surface is the HP surface as shown in Fig. 15. The height is 1.8 m and projected shape onto xy -plane is a 3×3 m square. The triangulation pattern and the planes of symmetry are shown in Fig. 16, and the DOF of the mechanism of the initial shape is 37. S_j is also used in this subsection to select the crease line to be fixed. The number of the independent variables in the optimization is the same as in the examples in Section 6.5. The results of the form generation are shown in Table 8. They have the same tendency as the results of the dome surface.

Fig. 17 shows the 3-DOF optimal shape obtained by considering the sym-

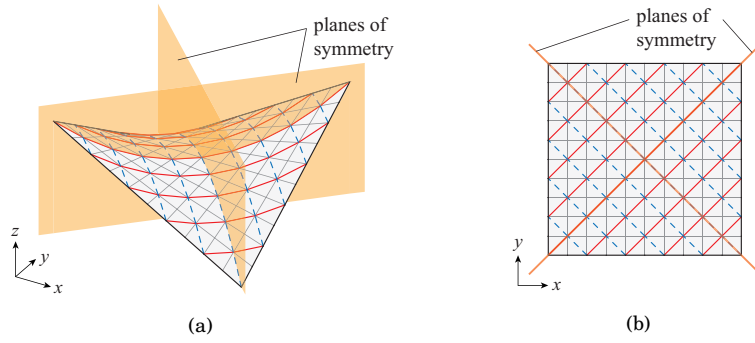


Figure 16: Initial triangulation and planes of symmetry: (a) isometric projection; (b) projection onto xy -plane

Table 8: Results of form generation for the dome surface

	symmetry	asymmetry
N_{lock}	0	0
N_{exceed}	0	0
Min. DOF	3	1
No. of opt.	10	37
Ave. $F(\mathbf{X})$	2.60×10^{-9}	1.72×10^{-9}
Ave. $D(\mathbf{X}^d)$	1.08×10^{-10}	9.18×10^{-10}
Ave. $ \Delta l_j $ [mm]	0.279	0.286
Ave. $ \Delta \rho_j^{\text{fix}} $ [deg.]	1.44×10^{-2}	2.19×10^{-2}

metry condition, which does not contain any locked crease line. The optimal objective values of $F(\mathbf{X})$ and $D(\mathbf{X}^d)$ of this solution are 1.69×10^{-9} and 9.19×10^{-11} , respectively, and the development diagram can be generated with good accuracy as shown in Fig. 17(c). The average values of $|\Delta l_j|$ ($j = 1, \dots, E$) and $|\Delta \rho_j^{\text{fix}}|$ ($j \in E_{\text{fix}}$) throughout the process of large-deformation analysis are 0.434 mm and 1.28×10^{-2} deg., respectively. Therefore, it can be concluded that the optimal shape shown in Fig. 17 is developable to a plane and practically rigid-foldable.

When the symmetry is considered, the average computation times for solving the optimization problems (6) and (13), performing the large deformation analysis, and selecting the crease lines to be fixed are 218 sec., 1.65 sec., 48.5 sec., 1.01 sec., respectively. The total computation time to obtain the 10 solutions is 2687 sec.. On the other hand, when the symmetry is not considered, the average computation times are 1133 sec., 19.3 sec., 57.3 sec., and 0.874 sec., respectively, and the total computation time to obtain the 37 solutions is 44771 sec..

Although the computation time highly depends on the implementation of the program, according to Table 4, it tends to increase as the model becomes more complex. If we assume the average computation time for solving the problem (6) is proportional to the square of the number of independent variables, the coefficients for the models in Sections 6.3 ~6.6 without considering symmetry conditions are 0.00895, 0.00832, 0.01165 and 0.01220, respectively. Therefore, the order is a little more than square of the number of independent variables. When the DOF of the initial shape is large, it is necessary to repeat the form generation process many times to reduce the DOF to the small value, and the total computation time considerably increases. Therefore, it is important to reduce the number of independent variables in the optimization problem utilizing the additional geometrical properties such as the symmetry conditions.

7. Conclusion

This paper has presented a form generation method of a developable rigid origami structure based on the mechanical property of partially rigid frames. A generated polyhedral surface approximates a target curved surface. Based on the method proposed in the authors' previous studies [19, 20, 21], form generation starts from a triangulated target surface and its crease lines are sequentially fixed to reduce the DOF of the deformation mechanism. The transition of the deformation mechanism due to fixing the crease lines is predicted, and selection criteria of the crease lines to be fixed are proposed to

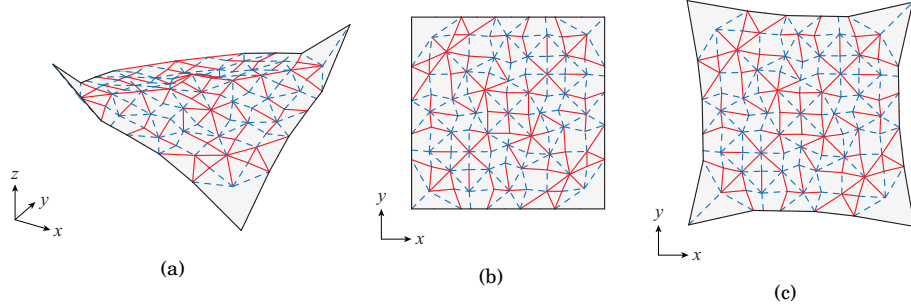


Figure 17: 3-DOF optimal shape for the target HP surface: (a) isometric projection; (b) projection onto xy -plane; (c) development diagram

prevent the unfixed crease lines from being locked. The deformation mechanism of rigid origami is investigated by using the frame model, and the deformation modes are derived by the method for stability and mechanism analysis of a partially rigid frame with arbitrary inclined hinges.

A procedure has been developed for detecting the existence of a locked crease line in the optimal shape after fixing a crease line based on the eigenvalue and eigenvector derivatives of the pseudo stiffness matrix of the frame model with respect to the fictitious rotational stiffness of the hinges (crease lines). The pseudo stiffness matrix of the frame is defined by the matrix of the hinge rotation modes and the diagonal matrix whose elements are the rotational stiffness of the hinges. Assuming that the eigenvalues of the pseudo stiffness matrix are distinct, the relationship between the eigenvalue derivatives and the eigenvector derivatives has been derived in Section 4 to show that a locked crease line likely exists if a crease line with the relatively small maximum eigenvalue derivative is fixed.

The selection criteria of the crease line to be fixed have been defined in consideration of both the convergence of the optimization for form generation and the possibility of the existence of a locked crease line. The convergence of the optimization is evaluated by the folding angles of the crease lines to be fixed, and the possibility of the existence of a locked crease line is evaluated by the maximum eigenvalue derivative or the maximum squared element of the orthonormalized rotation modes of the crease line to be fixed. Two selection criteria have been introduced, and their performances have been confirmed in numerical examples.

The form generation procedure has been carried out for 100 randomly generated target surfaces for each of the two crease patterns, i.e., in total 200 cases of form generation have been performed. Two selection criteria intro-

duced in this paper significantly reduce the number of times a crease line is locked in the form generation process in comparison to the case where the crease line to be fixed is selected based on the folding angle only or selected randomly. In addition, the optimal objective value representing the error of rigid folding is also reduced by using the introduced criteria. Therefore, it can be concluded that both the accuracy and the efficiency of form generation can be improved by considering both the geometry and the deformation mechanism of the rigid origami structure. Furthermore, comparing the two proposed criteria, the performance of the criterion defined by the orthonormalized hinge rotation modes is better than the other criterion defined by the eigenvalue derivatives of the pseudo stiffness matrix of the frame model.

Form generation has also been carried out for a dome surface and an HP surface to demonstrate applicability of the proposed method to the curved surface with positive and negative gaussian curvatures, respectively. The crease patterns in these examples are more complex than those in the examples of randomly generated target surfaces, and the symmetry conditions are considered in the optimization problem. The number of independent variables in the optimization problem can be reduced to about one quarter, and some crease lines are simultaneously fixed to reduce the multiple DOFs by assigning the symmetry conditions. However, the single-DOF optimal solutions could not be obtained for either of dome and HP surfaces. These examples have shown that the proposed method can be applied to any curved surface irrespective of the sign of Gaussian curvature.

Acknowledgements

This work is partly supported by JSPS KAKENHI Grant Number JP19K04714 and JST CREST Grant Number JPMJCR1911.

Appendix A. Derivation of compatibility equations

The method is summarized for constructing the compatibility equations (15) about nodal displacement of the frame model described in Section 4; see Refs. [27, 28] for details. The global coordinates (x, y, z) and the local coordinates of member k ($= 1, \dots, m$) of the frame model are defined as shown in Fig. A.1(a). As shown in Fig. A.1(b), the axial force and the torsional moment of member k are represented by N^k and T^k , respectively, and the bending moments around axes 2 and 3 at node $i \in \{1, 2\}$ are denoted by $M_{i,2}^k$ and $M_{i,3}^k$, respectively. The member-end shear forces are eliminated because they can be calculated from $M_{i,2}^k$ and $M_{i,3}^k$. These six indepen-

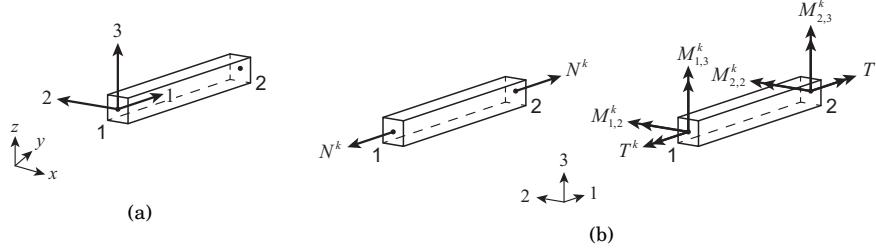


Figure A.1: Definition of member coordinates and member end forces: (a) local and global coordinates; (b) independent member-end forces

dent member-end forces of member k are combined into a vector $\mathbf{F}^k \in \mathbb{R}^6$ as: $\mathbf{F}^k = (N^k, T^k, M_{1,2}^k, M_{1,3}^k, M_{2,2}^k, M_{2,3}^k)^T$. The member-end force vector $\mathbf{F} \in \mathbb{R}^{6m}$ is defined as: $\mathbf{F} = (\mathbf{F}^{1T}, \dots, \mathbf{F}^{mT})^T$ whose elements are the member-end forces of all members in the frame model. When the frame model has n nodes and the number of constrained degrees of freedom of the nodal displacement is s , $6n - s$ equilibrium equations are derived. Defining $\mathbf{P} \in \mathbb{R}^{6n-s}$ and $\mathbf{S}_N \in \mathbb{R}^{(6n-s) \times 6m}$ as the nodal load vector and the equilibrium matrix, the equilibrium equations can be expressed as follows:

$$\mathbf{P} = \mathbf{S}_N \mathbf{F} \quad (\text{A.1})$$

If there are h hinges in the model, h equations are obtained representing the constraints of the moments around the rotation axes of hinges. Let $\mathbf{M} \in \mathbb{R}^h$ denote the vector whose elements are the designated moments around the axes of hinges. The constraints of the moment so that the axis of each component is directed to its corresponding hinge direction are expressed using the matrix $\mathbf{S}_R \in \mathbb{R}^{h \times 6m}$ as

$$\mathbf{M} = \mathbf{S}_R \mathbf{F} \quad (\text{A.2})$$

On the other hand, the following equation can be derived based on the principle of virtual work:

$$\mathbf{F}^T \mathbf{e} = \mathbf{P}^T \mathbf{u} + \mathbf{M}^T \boldsymbol{\varphi} \quad (\text{A.3})$$

where \mathbf{e} , \mathbf{u} , and $\boldsymbol{\varphi}$ represents the deformations of the members, the unconstrained displacements of nodes and the change of the rotation angle of the hinges, respectively. Assuming that \mathbf{e} can be represented by the linear combination of \mathbf{u} and $\boldsymbol{\varphi}$, \mathbf{e} can be expressed as Eq. (14) by substituting Eq. (A.1) and Eq. (A.2) into Eq. (A.3). Therefore, dividing \mathbf{S} into two components as

$\mathbf{S} = [\mathbf{S}_N^T \ \mathbf{S}_R^T]$, the compatibility equations are derived as Eq. (15) to ensure that the deformation of each member is zero.

Appendix B. Derivation of eigenvalue and eigenvector derivatives

The details of the derivation are presented below for the eigenvalue and eigenvector derivatives of the pseudo stiffness matrix $\tilde{\mathbf{K}}$ with respect to the rotation stiffness of the hinge. It is assumed that the eigenvalues λ_i ($i = 1, \dots, d$) are distinct. Differentiating Eq. (21) with respect to K_j ($j = 1, \dots, h$) and rearranging it yield:

$$(\tilde{\mathbf{K}} - \lambda_i \mathbf{I}) \frac{\partial \boldsymbol{\alpha}_i}{\partial K_j} = - \left(\frac{\partial \tilde{\mathbf{K}}}{\partial K_j} - \frac{\partial \lambda_i}{\partial K_j} \mathbf{I} \right) \boldsymbol{\alpha}_i \quad (i = 1, \dots, d) \quad (\text{B.1})$$

By pre-multiplying $\boldsymbol{\alpha}_i^T$ to the both sides of Eq. (B.1) and using Eq. (21) and $\tilde{\mathbf{K}}^T = \tilde{\mathbf{K}}$, the following equation is derived:

$$\boldsymbol{\alpha}_i^T \left(\frac{\partial \tilde{\mathbf{K}}}{\partial K_j} - \frac{\partial \lambda_i}{\partial K_j} \mathbf{I} \right) \boldsymbol{\alpha}_i = 0 \quad (i = 1, \dots, d) \quad (\text{B.2})$$

Hence, the derivative of eigenvalue λ_i with respect to K_j can be derived as Eq. (27) from the right side of Eq. (B.1).

Since the rank of $(\tilde{\mathbf{K}} - \lambda_i \mathbf{I})$ in the left-hand-side of Eq. (B.1) is less than $d - 1$, $\partial \boldsymbol{\alpha}_i / \partial K_j$ cannot be determined uniquely from Eq. (B.1). However, using a coefficient vector $\mathbf{c} = (c_1, \dots, c_d)^T \in \mathbb{R}^d$, it can be expressed as a linear combination of d orthonormal eigenvectors $\boldsymbol{\alpha}_i$ ($i = 1, \dots, d$) as follows [32]:

$$\begin{aligned} \frac{\partial \boldsymbol{\alpha}_i}{\partial K_j} &= c_1 \boldsymbol{\alpha}_1 + \dots + c_d \boldsymbol{\alpha}_d \\ &= [\boldsymbol{\alpha}_1 \quad \dots \quad \boldsymbol{\alpha}_d] \begin{pmatrix} c_1 \\ \vdots \\ c_d \end{pmatrix} \\ &= \mathbf{A} \mathbf{c} \end{aligned} \quad (\text{B.3})$$

Substituting $\partial \boldsymbol{\alpha}_i / \partial K_j = \mathbf{A} \mathbf{c}$ into Eq. (B.1), pre-multiplying \mathbf{A}^T to its both sides, and using Eq. (24), we derive the following equation to obtain \mathbf{c} :

$$\begin{aligned} \mathbf{A}^T (\tilde{\mathbf{K}} - \lambda_i \mathbf{I}) \mathbf{A} \mathbf{c} &= -\mathbf{A}^T \left(\frac{\partial \tilde{\mathbf{K}}}{\partial K_j} - \frac{\partial \lambda_i}{\partial K_j} \mathbf{I} \right) \boldsymbol{\alpha}_i \\ \Leftrightarrow (\Lambda - \lambda_i \mathbf{I}) \mathbf{c} &= -\mathbf{A}^T \left(\frac{\partial \tilde{\mathbf{K}}}{\partial K_j} - \frac{\partial \lambda_i}{\partial K_j} \mathbf{I} \right) \boldsymbol{\alpha}_i \end{aligned} \quad (\text{B.4})$$

Assuming $\lambda_k \neq \lambda_i$ ($k = 1, \dots, d$, $k \neq i$), c_k can be determined from Eq. (B.4) as follows by using $\boldsymbol{\alpha}_k^T \boldsymbol{\alpha}_i = 0$:

$$c_k = -\frac{1}{\lambda_k - \lambda_i} \boldsymbol{\alpha}_k^T \frac{\partial \tilde{\mathbf{K}}}{\partial K_j} \boldsymbol{\alpha}_i = -\frac{1}{\lambda_k - \lambda_i} \varphi_{ji} \varphi_{jk} \quad (\text{B.5})$$

In addition, c_i can be determined by differentiating $\boldsymbol{\alpha}_i^T \boldsymbol{\alpha}_i = 1$ with respect to K_j and dividing it by 2 as follows:

$$\frac{1}{2} \left\{ \left(\frac{\partial \boldsymbol{\alpha}_i}{\partial K_j} \right)^T + \boldsymbol{\alpha}_i^T \frac{\partial \boldsymbol{\alpha}_i}{\partial K_j} \right\} = \boldsymbol{\alpha}_i^T \mathbf{A} \mathbf{c} = c_i = 0 \quad (\text{B.6})$$

According to Eqs. (B.5) and (B.6), $\partial \boldsymbol{\alpha}_i / \partial K_j$ can be expressed as Eq. (29).

References

- [1] K. Miura, Method of packaging and deployment of large membranes in space, The Institute of Space and Astronautical Science report 618 (1985) 1–9.
- [2] K. Miura, Folded map and atlas design based on the geometric principle, in: Proceedings of the 20th International Cartographic Conference, Beijing, China, 2001.
- [3] K. Kuribayashi, K. Tsuchiya, Z. You, D. Tomus, M. Umemoto, T. Ito, M. Sasaki, Self-deployable origami stent grafts as a biomedical application of ni-rich tini shape memory alloy foil, *Materials Science and Engineering: A* 419 (1-2) (2006) 131–137. doi:10.1016/j.msea.2005.12.016.
- [4] P. M. Reis, F. L. Jimenez, J. Marthelot, Transforming architectures inspired by origami, *Proceedings of the National Academy of Sciences of the United States of America* 112 (40) (2015) 12234–12235. doi:10.1073/pnas.1516974112.
- [5] M. Kawaguchi, Design problems of long span spatial structures, *Engineering Structures* 13 (2) (1991) 144–163. doi:10.1016/0141-0296(91)90048-H.
- [6] N. D. Temmerman, M. Mollaert, T. V. Mele, L. D. Laet, Design and analysis of a foldable mobile shelter system, *International Journal of Space Structures* 22 (3) (2007) 161–168. doi:10.1260/026635107782218868.

- [7] T. Lee, J. M. Gattas, Geometric design and construction of structurally stabilized accordion shelters, *Journal of Mechanisms and Robotics* 8 (3) (2016) 031009–1–031009–8. doi:10.1115/1.4032441.
- [8] L. Dudte, E. Vouga, T. Tachi, L. Mahadevan, Programming curvature using origami tessellations, *Nature Materials* 15 (2016) 583–588. doi:10.1038/nmat4540.
- [9] K. Song, X. Zhou, S. Zang, H. Wang, Z. You, Design of rigid-foldable doubly curved origami tessellations based on trapezoidal crease patterns, *Proceedings of the Royal Society A: Mathematical, Physical and Engineering Sciences* 473 (2200) (2017) 20170016. doi:10.1098/rspa.2017.0016.
- [10] T. Tachi, Designing freeform origami tessellations by generalizing resch’s patterns, *Journal of Mechanical Design* 135 (11) (2013) 111066–1–111066–10. doi:10.1115/1.4025389.
- [11] R. D. Resch, Self-supporting structural unit having a series of repetitive geometrical modules (United States Patent No. 3,407,558, 1968).
- [12] Y. Zhao, Y. Endo, Y. Kanamori, J. Mitani, Approximating 3d surfaces using generalized waterbomb tessellations, *Journal of Computational Design and Engineering* 5 (2018) 442–448. doi:10.1016/j.jcde.2018.01.002.
- [13] J. Wu, Folding yoshimura pattern into large-scale art installation, in: R. J. Lang, M. Bolitho, Z. You (Eds.), *The proceedings from the 7th International Meeting of Origami Science, Mathematics, and Education (Origami7)*, Tarquin, 2018, pp. 1–13.
- [14] T. Tachi, Generalization of rigid foldable quadrilateral mesh origami, *Journal of the International Association for Shell and Spatial Structures* 50 (162) (2009) 173–179.
- [15] T. Tachi, Geometric considerations for the design of rigid origami structures, in: *Proceedings of the IASS Annual Symposium 2010, Shanghai, China, 2010*, pp. 8–12.
- [16] W. K. Schief, A. I. Bobenko, T. Hoffmann, On the integrability of infinitesimal and finite deformations of polyhedral surfaces, in: A. I. Bobenko, J. M. Sullivan, P. Schröder, P. M. Ziegler (Eds.), *Discrete Differential Geometry. Oberwolfach Seminars, Vol. 38*, Birkhäuser Basel, 2008, pp. 67–93.

- [17] Z. He, S. D. Guest, On rigid origami ii: Quadrilateral creased papers (2018). arXiv:1804.06483.
- [18] Z. He, S. D. Guest, Design of novel origami shell structures, in: Proceedings of the IASS Annual Symposium 2019, Barcelona, Spain, 2019, pp. 1055–1062.
- [19] K. Hayakawa, M. Ohsaki, Optimization approach to form generation of rigid-foldable origami for deployable roof structure, in: Proceedings of The World Congress of Structural and Multidisciplinary Optimization (WCSMO 13), Beijing, China, 2019, paper No. A050457.
- [20] K. Hayakawa, M. Ohsaki, Form generation of rigid-foldable origami structure using frame model, *Journal of Environmental Engineering (Transactions of AIJ)* 84 (760) (2019) 597–605, (in Japanese). doi:10.3130/aije.84.597.
- [21] K. Hayakawa, M. Ohsaki, Frame model for analysis and form generation of rigid origami for deployable roof structure, in: Proceedings of the IASS Annual Symposium 2019, Barcelona, Spain, 2019, pp. 1080–1087, paper No. 177.
- [22] J. M. Sullivan, Curvatures of smooth and discrete surfaces, in: A. I. Bobenko, J. M. Sullivan, P. Schröder, P. M. Ziegler (Eds.), *Discrete Differential Geometry. Oberwolfach Seminars, Vol. 38*, Birkhäuser Basel, 2008, pp. 175–188.
- [23] M. Schenk, S. D. Guest, Origami folding: A structural engineering approach, in: P. Wang-Iverson, R. J. Lang, M. Yim (Eds.), *Proceedings of the 5th International Meeting of Origami Science, Mathematics, and Education (Origami5)*, CBC Press, 2011, pp. 291–303.
- [24] E. T. Filipov, K. Liu, T. Tachi, M. Schenk, G. H. Paulino, Bar and hinge models for scalable analysis of origami, *International Journal of Solids and Structures* 124 (2017) 26–45. doi:10.1016/j.ijsolstr.2017.05.028.
- [25] T. Tachi, Simulation of rigid origami, in: R. J. Lang (Ed.), *Proceedings of the 4th International Meeting of Origami Science, Mathematics, and Education (Origami4)*, AK Peters, 2009, pp. 175–187.
- [26] N. Watanabe, Foldable condition in a singular state of a rigid origami model, *Transactions of the Japan Society for Industrial and Applied Mathematics* 28 (1) (2018) 54–71, (in Japanese). doi:10.1154/jsiamt.28.1_54.

- [27] S. Tsuda, M. Ohsaki, S. Kikukawa, Y. Kanno, Analysis of stability and mechanism of frames with partially rigid connections, *Journal of Structural and Construction Engineering (Transactions of AIJ)* 78 (686) (2013) 791–798, (in Japanese). doi:10.3130/aijs.78.791.
- [28] M. Ohsaki, S. Tsuda, Y. Miyazu, Design of linkage mechanisms of partially rigid frames using limit analysis with quadratic yield functions, *International Journal of Solids and Structures* 88-89 (2016) 68–78. doi:10.1016/j.ijsolstr.2016.03.023.
- [29] E. D. Demaine, J. O’Rourke, *Geometric folding algorithms: linkages, origami, polyhedra*, Cambridge University Press, 32 Avenue of the Americas, New York, NY 10013-2473, USA, 2007.
- [30] C. C. L. Wang, S. S.-F. Smith, M. M. F. Yuen, Surface flattening based on energy model, *Computer-Aided Design* 34 (2002) 823–833. doi:10.1016/S0010-4485(01)00150-6.
- [31] C. Meyer, *Matrix Analysis and Applied Linear Algebra*, SIAM, 3600 University City Science Center Philadelphia, PA, United States, 2000.
- [32] R. B. Nelson, Simplified calculation of eigenvector derivatives, *AIAA Journal* 14 (9) (1976) 1201–1205. doi:10.2514/3.7211.
- [33] G. Farin, *Curves and Surfaces for CAGD: A Practical Guide*, 5th Edition, Morgan Kaufmann Publishers Inc., San Francisco, CA, USA, 2001.
- [34] D. Systèmes, Abaqus 2016 online documentation, <http://abaqus.software.polimi.it/v2016/> (2015).